

REPORT DOCUMENTATION PAGE

Form Approved
OMB No. 0704-0188

Public reporting burden for this collection of information is estimated to average 1 hour per response, including the time for reviewing instructions, searching existing data sources, gathering and maintaining the data needed, and completing and reviewing the collection of information. Send comments regarding this burden estimate or any other aspect of this collection of information, including suggestions for reducing the burden, to Washington Headquarters Services, Directorate for Information Operations and Analysis, 1215 Jefferson Davis Highway, Suite 1200, Arlington, VA 22202-4302, and to the Office of Management and Budget, Paperwork Reduction Project (0704-0188), Washington, DC 20585.

1. AGENCY USE ONLY (Leave blank)	2. REPORT DATE	3. REPORT TYPE AND DATES COVERED
	7/31/95	Final Technical Report 8-1-92--7-31/95

4. TITLE AND SUBTITLE

(U) PARTICLE DISPERSION IN TURBULENT SPRAYS

5. FUNDING NUMBERS

PE - 61102F
PR - 2308
SA - BS
G - F49620-92-J-0418

6. AUTHOR(S)

IAN M. KENNEDY AND WOLFGANG KOLLMANN

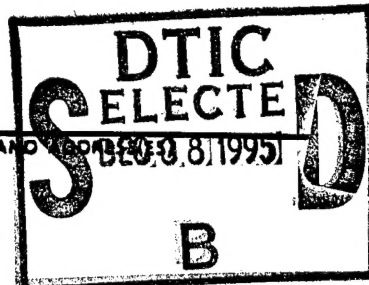
7. PERFORMING ORGANIZATION NAME(S) AND ADDRESS(ES)

UNIVERSITY OF CALIFORNIA
DAVIS, CA 95616

8. PERFORMING ORGANIZATION REPORT NUMBER

AFOSR-TR-95
0780

9. SPONSORING/MONITORING AGENCY NAME(S) AND ADDRESS(ES)

AFOSR/PKA
110 Duncan Avenue, Suite B115
Bolling AFB, DC 20332-0001

10. SUPPLEMENTARY NOTES

12a. DISTRIBUTION/AVAILABILITY STATEMENT

Approved for public release; distribution is unlimited

12b. DISTRIBUTION CODE

13. ABSTRACT (Maximum 200 words)

A Large Eddy Simulation (LES) was used to model a two phase turbulent round jet. The LES for the continuous phase used the Smagorinsky model for the sub-grid-scale motion. A simple model for the effect of the particles on the continuous phase was developed. The model was essentially a momentum balance for a fluid volume containing particles moving relative to the continuous phase. The simulation showed that particles accelerated the roll-up of the shear layer. Droplet dispersion was measured in a turbulent round jet of air issuing into still air. Individual droplets were formed with a piezo-electric device; they were injected onto the centerline of the jet. Their location across the jet was measured at different axial stations with a laser sheet and position sensing photomultiplier tube. Particles containing a fluorescent dye were injected into a turbulent spray. Spray scattering was rejected with a Raman filter. Dispersion of the tagged particles was measured. Results agreed with the LES in which the injection of the spray enhanced development of the jet and the dispersion of particles.

DTIC QUALITY INSPECTED 1

14. SUBJECT TERMS

TURBULENCE, SPRAYS, PARTICLE DISPERSION

15. NUMBER OF PAGES

51

16. PRICE CODE

17. SECURITY CLASSIFICATION OF REPORT

Unclassified

18. SECURITY CLASSIFICATION OF THIS PAGE

Unclassified

19. SECURITY CLASSIFICATION OF ABSTRACT

Unclassified

20. LIMITATION OF ABSTRACT

UL

PARTICLE DISPERSION IN TURBULENT SPRAYS

AFOSR Grant G-F49620-92-J-0418

Final Report: 5/15/92 to 5/14/95.

Principal investigators: I.M. Kennedy and W. Kollmann

Department of Mechanical & Aeronautical Engineering
University of California, Davis, CA 95616

Table of contents.

1.0	Executive Summary.	3
1.1	Computational Approach.	5
1.1.1	Large Eddy Simulation.	6
1.1.2	Spray simulations.	8
1.1.3	Time integration schemes.	13
1.2	Experimental Approach.	15
1.2.1	Dispersion in a Spray.	16
1.3	References	17
	Appendix	21

1.0 Executive Summary.

Experiment.

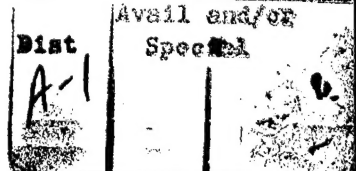
Particle dispersion and particle velocities were measured with laser sheets and a position sensitive photo multiplier tube to track particles. Monodisperse hexadecane droplets were injected onto the centerline of a turbulent air jet. Their radial dispersion, axial velocities, and times of flight were measured as functions of axial position. The time and length scales of the jet were varied through the control of the jet exit velocity and nozzle diameter. Nozzle diameters of $7 \mu m$ and $12.6 \mu m$ were used. Reynolds numbers were in the range of 10,000 to 32,400. Two different droplet diameters were used viz., $60 \mu m$ and $90 \mu m$. A significant range in the Kolmogorov, turbulent, and acceleration Stokes numbers was covered. The times-of-flight were used to analyze the dispersion measurements in terms of true Lagrangian statistics. It was found that the use of a mean time of flight to present the data incurred quite small errors relative to the exact Lagrangian statistics. Dispersion data for long times flight over the range of nozzle diameters, particle diameters and exit velocities were analyzed to obtain the Lagrangian particle diffusivity. The non-dimensional diffusivities or Peclet numbers were found to approach a value that was similar to the Eulerian Peclet number for scalar transport in the jet. Furthermore, the dispersion increased linearly with time. The results suggested that some economies could be achieved in the simulation of dilute, two phase turbulent jets and similar flows over times long in comparison to the Lagrangian integral length scale by taking advantage of their self preserving nature.

An additional goal of the experiments was to measure the dispersion of tagged droplets in a Lagrangian sense within a turbulent spray. A modified experimental apparatus was designed to this end. Individual droplets were tagged with a fluorescent dye. The tagged droplets were injected into a round turbulent jet into which a dispersed, liquid spray had been added. The location of the tagged particle was followed through the jet with an optical detection system that was a modification of an earlier technique. This experimental approach provided a simple two phase flow with well defined boundary conditions without the significant complications that are introduced by spray atomization.

Sprays with mass loadings from 0 up to 7% were added to the jet. The signal to noise ratio under these conditions was about 110. The mean square displacement of the fluorescent droplet was measured at varying x/D from the exit of the nozzle. It was apparent that the spray contributes to the breakdown of the jet with larger spray loadings, resulting in greater dispersion of the tagged fluorescent droplets that were added to the flow. The results were compared with the predictions of a Large Eddy Simulation (LES) and were found to be encouraging.

Theory and Computation.

The flow field in turbulent round jets and the paths of droplets ranging from fluid material points to heavy particles (hexadecane droplets) were simulated numerically. The large scale structures of the flow field were resolved and the scales smaller than the grid were modelled using the LES approach. The particles were tracked individually in the Lagrangian frame and the influence of the particles on the fluid phase was represented using the PIC (particle source in cell) method.



The simulation of particle laden turbulent jets allowed the computation of correlation functions for particles and fluid phase not accessible to single point turbulence closures. The present LES model for the turbulent jet produced results for the auto-correlation function of the particle velocities in good agreement with measurements for the case of axial velocity components shifted in time.

The numerical simulation of dilute sprays was performed to investigate the effect of the spray on the near field of a turbulent jet at a moderate Reynolds number $Re = 10,000$. The dispersion of tagged particles was measured and simulated numerically. The effect of the spray on the flow structure emerged as reduction in the size of the largest vortices and an increase in their number in the initial region of the jet.

The finite-difference method for the simulation of the fluid phase dynamics was improved in several aspects. The original Adams-Basforth time integration scheme was second order accurate and unstable in the inviscid case. Runge-Kutta schemes of third and fourth order accuracy were explicit and conditionally stable. Development of both variants was begun and they were first implemented into the two-dimensional Navier-Stokes solvers for plane and axisymmetric flows with excellent results. The discretization of the convective terms was extended to windward biased schemes up to seventh order and successfully implemented into the Runge-Kutta versions of the two-dimensional and axisymmetric Navier-Stokes solvers.

Personnel.

The following persons have been supported under this grant: Professor Ian Kennedy, Principal Investigator; Professor Wolfgang Kollmann, Co-principal Investigator; Dr. Charles Call, PhD student; Dr. Jeff Lienau, PhD student; Dr. Clement Yam, Postdoctoral researcher; Mr. Michael Moody, MS student; Mr. Philip Santangelo, PhD candidate; Mr. Michael White, PhD candidate.

Publications.

- D. Hansell, I. M. Kennedy and W. Kollmann, "A Simulation of Particle Dispersion in a Turbulent Jet", Int. J. Multiphase Flow 18, 559 - 576 (1992).
- C. Call and I. M. Kennedy, "Measurements and Simulations of Particle Dispersion in a Turbulent Flow", Int. J. Multiphase Flow, 18, 891 - 903 (1992).
- C. Call and I. M. Kennedy, "Velocity, Vaporization and Dispersion of Droplets in Heated and Unheated Turbulent Jets", AIAA Aerospace Sciences Meeting, Paper 93-0904, Reno NV 1993.
- J. Lienau, W., Kollmann and I. M. Kennedy, "Large Eddy Simulations of Particle Dispersion in a Turbulent Jet", AIAA Aerospace Sciences Meeting, Reno, NV 1993.
- C. Call and I. M. Kennedy, "Measurements of Droplet Dispersion in Heated and Unheated Turbulent Jets", A.I.A.A. J. 32, No. 4, 874 - 875, April 1994.
- C. Call, PhD Thesis[†] "Particle dispersion in turbulent shear flows", University of California, Davis 1992

[†] Theses may be obtained from Graduate Studies, University of California, Davis, CA 95616

J. J. Lienau, PhD Thesis, "Direct and Large Eddy Simulations of Three Dimensional Round Turbulent Jets", University of California, Davis 1994

M. H. Moody, MS Thesis, "An investigation of time and length scale effects on particle dispersion in a turbulent shear flow", University of California, Davis 1994.

J. J. Lienau, I. M. Kennedy and W. Kollmann, "Numerical Simulation of Vaporizing Particles in Turbulent Jets", Paper 94-0662, AIAA Aerospace Sciences Meeting, Reno NV. Jan. 1994.

C. Yam, C. Romero, W. Kollmann, I. M. Kennedy and J. J. Lienau, "The Effect of a Spray on Particle Dispersion in the Near Field of a Round Jet", Paper 95-0384 AIAA Aerospace Sciences Meeting, Reno NV January 1995.

I. Kennedy and M. Moody, "Particle Dispersion in a Turbulent Round Jet", submitted to Physics Fluids

1.1 Computational Approach.

The Navier-Stokes equations were solved using an accurate finite-difference method discussed in detail in Lienau and Kollmann (1993) and the final report (1989/92) for AFOSR Grant no. 89-0392. The void fraction for dilute sprays was approximated by unity and the Navier-Stokes equation have then the usual form for incompressible flows. The original method proceeded in two steps: First the momentum balances were solved in the predictor step. The predicted velocities did not satisfy mass balance and a second step was necessary to correct velocity and pressure. In this second step a Poisson equation for the pressure correction was solved and velocity and pressure were updated.

Momentum and mass balances were set up in cylindrical coordinates (r, θ, ζ) and were discretized using accurate finite difference expressions. Simple grid stretching transformations were applied to the $r = r(\bar{r}, \beta)$ and $\zeta = \zeta(\bar{\zeta}, \beta)$ directions ($\beta > 1$ denotes the stretching parameter, Lienau and Kollmann, 1993) to concentrate the grid points in the region of interest and to move the outer boundary as far out as possible without wasting too many grid points. The time derivative was discretized using the second order accurate three point backward (Adams Bashforth) scheme. The convective terms were discretized to second order accuracy using a four point windward biased compact differencing scheme (Rai and Moin, 1991). The pressure gradient was discretized to fourth order accuracy using the three point central compact scheme (Lele, 1990) and the viscous terms were discretized to fourth order accuracy using five point central differencing.

Mass balance was enforced using the pressure correction method. A hybrid method was developed for the solution of the Poisson equation for the pressure correction that exploits the periodicity of the flow field in circumferential θ -direction. It consisted of a fourth order compact central finite difference scheme for the nonperiodic dependence on axial and radial coordinates, that allowed the application of a direct solver, and a Fourier spectral method in the periodic θ direction. The direct solver had the advantage that it provided the solution in a fixed number of computational steps per time step and it was more efficient for large problems than iterative methods.

The present simulation method was not able to resolve all scales of turbulence and a Sub-Grid-Scale (SGS) viscosity model was added to represent the effect of the unresolved scales of motion on the resolved ones (Reynolds, 1990). The Navier-Stokes equations

were written for filtered variables using the top hat filter. The closure for the additional correlations was completed by neglecting the sum of Leonard and cross stresses and the Smagorinsky model was applied to the SGS stresses. The top hat filter corresponded precisely to the integration for the force term representing the effect of the particles on the fluid phase (see section 1.1.2). The details of the LES approach were described in section 1.1.1.

Boundary and initial conditions were critical for validity of the simulation. The jet issuing into stagnant surroundings operated in an infinite domain with the boundary condition that velocity was integrable. This situation was approximated by a cylindrical domain with radius much larger than the jet pipe and by conditions at the outer boundary that did not affect the flow in the jet significantly. After many trials a condition was found that worked reasonably well: Set the normal derivative of velocity to zero on the outer part of the boundary. The centerline was not a boundary, since a point on $r = 0$ was inner point of the flow field. The finite difference grid could have been set up such that the axis $r = 0$ was gridline, which required a detailed analysis of the equations at this gridline to remove singularities introduced by the metric of the coordinate system, or such that $r = 0$ was between grid surfaces. The latter method was chosen since it was straightforward to implement.

The pressure gradient in the direction normal to the computational boundary was set to zero at the jet inlet and exit planes. On the outer boundary the pressure and the pressure correction were set to zero. This provided stability for the jet without affecting the solution appreciably. The inlet condition for the jet was obtained using the experimental results of Call and Kennedy (1991) or Liepmann (1991) and Liepmann and Gharib (1992) and the entire flow field was initialized with the inlet profile, representing an inviscid flow initially. This type of initial condition was superior to starting the jet flow by increasing the mass flow rate until the desired steady state value was reached. The flow set up this way was first dominated by the start up vortex, which moves through the flow field creating an axial flow similar to the inviscid initial condition, but requires significantly more CPU-time without significant change of the later flow development.

Disturbances were introduced at the inlet to initiate and accelerate the roll-up process of the cylindrical shear layer. The disturbance $\tilde{v}_\zeta(\theta, t)$ was chosen such that it was only a function of θ and time similar to Rai and Moin (1991) and satisfies, therefore, mass balance. It was given by

$$\tilde{v}_\zeta = \sum_{k=1}^K \sum_{n=1}^N A_{l,n} \sin(k\theta + \phi_\theta) \sin\left(\frac{2\pi nt}{\tau} + \phi_t\right) \quad (1)$$

where $A_{l,n} = cv_{jet}r_{jet}\delta^{k-1}\gamma^{n-1}$, $\delta = 0.25$, $\gamma = 0.5$, $c = 0.1$. Two modes in both θ and time were selected (i.e. $K = 2, N = 2$).

The analysis for the Adams Bashforth time integration method and the compact four point windward biased scheme for the convective terms revealed that the maximum stable Courant number was 0.5. Combining the time step restrictions for convective and viscous terms lead to the maximal time step

$$\Delta t \leq 0.5 \left[\min_{\underline{x}} \frac{\partial \bar{r}}{\partial r} \frac{|v_r|}{\Delta \bar{r}} + \frac{1}{r} \frac{|v_\theta|}{\Delta \theta} + \frac{\partial \bar{\zeta}}{\partial \zeta} \frac{|v_\zeta|}{\Delta \bar{\zeta}} + \frac{1}{3Re} \left(\left(\frac{\partial \bar{r}}{\partial r} \right)^2 \frac{1}{\Delta \bar{r}^2} + \frac{1}{r^2 \Delta \theta^2} + \left(\frac{\partial \bar{\zeta}}{\partial \zeta} \right)^2 \frac{1}{\Delta \bar{\zeta}^2} \right) \right]^{-1} \quad (2)$$

which was used to control the time step.

1.1.1 Large Eddy Simulation

The Large Eddy Simulation of the turbulent flow in round jets was the most realistic approach for the prediction of the statistical properties of the flow field and the simulation of Lagrangian particle dynamics in this type of flow, since direct simulation of turbulence in round jets at high Reynolds numbers was still not within the capabilities of present computers. The simulation of turbulent flow fields in round jets in the present project was based on highly accurate finite-difference methods, which offer the flexibility necessary for the treatment of non-periodic jet flows emitting from nozzles and the consideration of a variety of exit geometries and velocity profiles. Furthermore, the influence of disturbances created at the jet pipe exit on the flow development was able to be studied in detail. This aspect of the project was described in detail in the final report for grant AFOSR 89-0392 and further details can be found in Lienau, Kennedy and Kollmann (1993) and Lienau and Kollmann (1993) of the publication list.

The accomplishments of the current review period covered the implementation of the LES model and improvements of the solution procedure. The numerical treatment of the coordinate axis $r = 0$ for unsteady flows without symmetries was analyzed (details in the appendix of the annual report for 1992/3) and a satisfactory method was found to avoid the loss of accuracy near the axis. The second and main contribution was the implementation of a LES-model for the non-resolved scales of the turbulence. The Navier-Stokes equations are written for filtered variables

$$\bar{f}(\underline{x}, t) \equiv \int d\underline{x}' G(\underline{x} - \underline{x}', t) f(\underline{x}', t) \quad (3)$$

where $G(\underline{x} - \underline{x}', t)$ denotes the filter function and $f(\underline{x}, t)$ a dependent variable. The Navier-Stokes equations (in Cartesian coordinates for convenience) were filtered and emerge as

$$\frac{\partial \bar{v}_\alpha}{\partial x_\alpha} = 0 \quad (4)$$

and

$$\frac{\partial \bar{v}_\alpha}{\partial t} + \frac{\partial}{\partial x_\beta} (\bar{v}_\alpha \bar{v}_\beta) = -\frac{1}{\rho} \frac{\partial \bar{P}}{\partial x_\alpha} + \nu \frac{\partial^2 \bar{v}_\alpha}{\partial x_\beta \partial x_\beta} - \frac{\partial}{\partial x_\beta} (L_{\alpha\beta} + C_{\alpha\beta} + R_{\alpha\beta}) \quad (5)$$

The modified filtered pressure was defined by

$$\bar{P} \equiv \bar{p} + \frac{1}{3} \rho \delta_{\alpha\beta} \bar{v}'_\alpha \bar{v}'_\beta \quad (6)$$

and the correlations of filtered and sub-grid-scale motion ($v'_\alpha = v_\alpha - \bar{v}_\alpha$) were given by

$$L_{\alpha\beta} \equiv \overline{\bar{v}_\alpha \bar{v}_\beta} - \bar{v}_\alpha \bar{v}_\beta \quad (7)$$

$$C_{\alpha\beta} \equiv \overline{v'_\alpha \bar{v}_\beta} + \overline{\bar{v}_\alpha v'_\beta} \quad (8)$$

$$R_{\alpha\beta} \equiv \overline{v'_\alpha v'_\beta} - \frac{1}{3} \delta_{\alpha\beta} \overline{v'_\gamma v'_\gamma} \quad (9)$$

The present filter was the top hat filter and the closure for the correlations is given by

$$L_{\alpha\beta} + C_{\alpha\beta} \approx 0 \quad (10)$$

and the Smagorinsky model for $R_{\alpha\beta}$ (Reynolds, 1990)

$$R_{\alpha\beta} \equiv -2\nu_T S_{\alpha\beta} \quad (11)$$

where the eddy-viscosity was defined by

$$\nu_T \equiv (c\Delta)^2 (2S_{\alpha\beta} S_{\alpha\beta})^{\frac{1}{2}} \quad (12)$$

and

$$\Delta \equiv (\Delta x \Delta y \Delta z)^{\frac{1}{3}} \quad (13)$$

and

$$S_{\alpha\beta} \equiv \frac{1}{2} \left(\frac{\partial \bar{v}_\alpha}{\partial x_\beta} + \frac{\partial \bar{v}_\beta}{\partial x_\alpha} \right) \quad (14)$$

was the rate of strain produced by the filtered velocity field.

The sub-grid-scale model (10) to (14) had a significant effect on the structure of the flow of the fluid phase and on the motion of the particles suspended in it. The simulation of the turbulent flow in the round jet for the conditions of the experiments by Call and Kennedy (1991) at the nominal Reynolds number of $Re = 15,000$ proved this point. Figure 1 and 2 show the distribution of the absolute value of vorticity in the section $\theta = 0/\pi$ with and without the SGS model in the axial range $0 \leq \frac{x}{D} \leq 60$. The constant c in (12) was set to zero in Figure 1 and the discretization error plays then the role of the filter (Boris, 1990), whereas $c = 0.025$ for the Smagorinsky model (11) in Figure 2. It was evident that the LES-model using the eddy viscosity (10) dampens the smaller scales and reduces the scale range. It turns out that the spreading rate in the LES case was in very good agreement with the experimental evidence. More importantly, the effect of the LES-model on the particle statistics was also beneficial as the following figures proved. The dispersion of $113\mu m$ pentane particles in the heated jet (temperature difference at jet pipe exit: $60^\circ K$) as function of the axial distance in Figure 3 showed excellent agreement between measurement and numerical simulation with the LES-model. Preliminary results for the auto-correlation function of the axial velocity component of lighter ($50\mu m$ hexadecane) particles in Figure 4 showed also close agreement with the experiments of Call and Kennedy (1991). The calculation of the time of flight plays a noticeable role for dispersion as Figure 5 illustrated. The experiment was limited to the mean time of flight, whereas the numerical simulation allowed the computation of individual times of flight. It was evident from Figure 5 that the dispersion calculated with the experimental (mean) time of flight was much closer to the measurements. The effect of the LES-viscosity on the dispersion was shown in Figure 6. The increase in viscosity due to the LES-model (10) decreased the dispersion and improved the agreement with the measurements. Finally, it was found that the mean particle velocity in axial direction was fairly independent of the method of calculating the time of flight.

1.1.2 Spray simulations.

The turbulent jet used in the experiment for the study of droplet dispersion had a sufficiently low Mach number such that the flow of an incompressible fluid containing particles was considered incompressible for the numerical simulations. The Navier-Stokes equations for the incompressible fluid phase were set up for the conditions of a flow laden with fine particles. The volume occupied by the particles per unit volume denoted by $\theta(\underline{x}, t)$ was defined by

$$\theta(\underline{x}, t) = \lim_{V \rightarrow V_0} \left(1 - \frac{V_p}{V}\right) \quad (15)$$

where V was the volume of a subdomain \mathcal{D} of the flow field, that was contracted to the limit \mathcal{D}_0 centered at the point \underline{x} , and V_p was the volume of all particles \mathcal{D}_i in \mathcal{D} . The limit value V_0 for the subdomain \mathcal{D} in (5) for dilute sprays of particles much smaller than the smallest length scale of the flow can be chosen sufficiently small, such that the void fraction can be regarded as local variable. The limit was then well defined and the void fraction emerged for spherical particles in the form (Dukowicz, 1980)

$$\theta(\underline{x}, t) = 1 - \sum_{i=1}^{N(\underline{x})} \frac{4\pi}{3} \frac{r_i^3}{V_0} \quad (16)$$

where the sum extends over all particles in \mathcal{D}_0 and $N(\underline{x})$ was the number of particles in \mathcal{D}_0 centered at \underline{x} . The mass balance for the two-phase system had then the form (Dukowicz, 1980)

$$\frac{\partial \theta}{\partial t} + \frac{\partial}{\partial x_\alpha} (\theta v_\alpha^f) = 0$$

and momentum balance was given by

$$\frac{\partial v_\alpha^f}{\partial t} + v_\beta^f \frac{\partial v_\alpha^f}{\partial x_\alpha} = -\frac{1}{\rho^f} \frac{\partial p}{\partial x_\alpha} + \frac{1}{\theta} \frac{\partial}{\partial x_\beta} (\theta \nu^f \frac{\partial v_\alpha^f}{\partial x_\beta}) + g_\alpha + \frac{1}{\theta} M_\alpha$$

where the superscript f indicated the fluid phase. The last term in the momentum balance represented the effect of the particles on the fluid momentum as defined below. The case of dilute sprays of small particles was considered in the following, where the approximations were made: the particle size was much smaller than the smallest length scale of the flow and that $\theta = 1.0$ holds. Hence, the displacement effect of the particles was neglected, but not the forces exerted by the particles on the fluid. The Navier-Stokes equations emerged then in the form (Elghobashi and Truesdell, 1991, 1993, Eaton, 1994)

$$\frac{\partial}{\partial x_\alpha} (v_\alpha^f) = 0 \quad (17)$$

Momentum balance

$$\frac{\partial v_\alpha^f}{\partial t} + v_\beta^f \frac{\partial v_\alpha^f}{\partial x_\alpha} = -\frac{1}{\rho^f} \frac{\partial p}{\partial x_\alpha} + \frac{\partial}{\partial x_\beta} (\nu^f \frac{\partial v_\alpha^f}{\partial x_\beta}) + g_\alpha + M_\alpha \quad (18)$$

which contained the effect M_α of the particles on the fluid phase.

Particle dynamics.

Solid spherical particles in a gaseous fluid phase were considered. The position of particle p at time t was denoted with $\underline{X}^p(t)$ and its velocity with $\underline{v}^p(t)$. The position and velocity of a particle were related by definition

$$\frac{d\underline{X}_\alpha^p}{dt}(t) = \underline{v}_\alpha^p(\underline{X}^p(t), t) \quad (19)$$

with the initial condition $\underline{X}^p(0) = \underline{x}^p$ (\underline{x} denoted the release position of particle p). The particle velocity $\underline{v}^p(t)$ was different from the Eulerian velocity field $\underline{u}^f(\underline{x}, t)$ of the fluid phase, which was the solution of the Navier-Stokes equations (17), (18) obtained with the finite-difference method described in a later section. The dynamic equation determining the location of particles with nonzero mass was a consequence of Newton's second law with approximations for the forces acting on the particle (see Odar and Hamilton, 1964). The equation for the particle velocity contained terms representing drag and virtual mass, the Basset term and buoyancy.

$$\begin{aligned} \frac{d\underline{u}^p}{dt} = & \frac{3C_D}{4d} \frac{\rho_f}{\rho_p} |\underline{u}^f - \underline{u}^p| (\underline{u}^f - \underline{u}^p) + \frac{1}{2} \frac{\rho_f}{\rho_p} C_I \frac{D}{Dt_p} (\underline{u}^f - \underline{u}^p) + \frac{\rho_g}{\rho_p} \frac{Du^f}{Dt_f} \\ & + \frac{9}{d} \frac{\rho_g}{\rho_p} \left(\frac{\nu}{\pi} \right)^{\frac{1}{2}} C_B \int_{t_0}^t \frac{d\tau}{(t-\tau)^{\frac{1}{2}}} \frac{D}{Dt_p} (\underline{u}^f - \underline{u}^p) + \left(\frac{\rho_g}{\rho_p} - 1 \right) \underline{g} \end{aligned} \quad (20)$$

The subscript f denoted fluid (gas) and p particle properties, the substantial derivatives were to be taken accordingly as following a material point of the fluid or the particle, d was the particle diameter, ν was the gas viscosity and \underline{u}^f , ρ_f were taken as the values undisturbed by the particle at the location of the particle. The coefficients C_D , C_I and C_B were in general functions of the particle Reynolds number

$$Re_p \equiv \frac{|\underline{u}^f - \underline{u}^p| d}{\nu} \quad (21)$$

and the acceleration number (see Faeth, 1983 and Hansell et al., 1992)

$$An \equiv \frac{\frac{D}{Dt_p} |\underline{u}^f - \underline{u}^p|}{|\underline{u}^f - \underline{u}^p|^2} d \quad (22)$$

The drag coefficient was given by (Putnam, 1961)

$$C_d = \frac{24}{Re} \left(1 + \frac{Re_p^{\frac{2}{3}}}{6} \right) \quad \text{for } Re_p < 1000 \quad (23)$$

The present calculation of the particle dynamics took only drag, virtual mass and buoyancy into account. The Basset term was rather expensive to calculate and will be implemented at a later stage. Therefore, particle velocity was the solution of

$$\frac{d\underline{u}_p}{dt} = \frac{3}{4} \frac{C_D}{d} \frac{\rho_g}{\rho_p} |\underline{u}_g - \underline{u}_p| (\underline{u}_g - \underline{u}_p) + \frac{\rho_g}{\rho_p} \frac{Du_g}{Dt_g} + \left(\frac{\rho_g}{\rho_p} - 1 \right) \underline{g} \quad (24)$$

For the present computations the properties for $d = 36 \mu M$ liquid hexadecane particles were used, which were given by $\rho_p = 775 \frac{kg}{m^3}$. The relevant properties of air were $\nu = 1.45(10)^{-5} \frac{m^2}{s}$, $\rho_g = 1.19 \frac{kg}{m^3}$.

The time integration for (19) and (20) was carried out simultaneously with the integration of the Navier-Stokes equations. The second order accurate improved Euler method was applied to the time integration of the particle equations, which was the same order of accuracy as the current time integration scheme for the Navier-Stokes equations. The values of velocity at an arbitrary location inside a grid cell were required for this integration method. They were interpolated using a second order polynomial (Bezier Spline) in three dimensions. This involved using a three point stencil consisting of the two points defining the cell containing the particle location and the point ahead or behind this cell depending which point was closest. The three dimensional interpolation scheme was rather complicated and only the overall Bezier spline in one dimension will be given

$$\psi_p = \frac{1}{c}(a^2\psi_{j-1} + 2ab\psi_j + b^2\psi_{j+1}) \quad (25)$$

where ψ was the variable being interpolated, a was the distance from the particle to point $j + 1$ and b was the distance from the particle to the point $j - 1$ and c was the distance from point $j - 1$ to $j + 1$ and the particle is between $j - 1$ and j .

Interaction of fluid and particles

The particle dynamics were driven by the forces exerted by the fluid phase on the particles. The effect of the particles on the fluid phase was represented by the force term \underline{M} in the momentum balance (18) and the displacement effect of the particles described by the void fraction. If the momentum balance (24) for the particles was written as

$$\frac{du^p}{dt} = \underline{F}^p \quad (26)$$

where \underline{F}^p was the sum of all forces acting on a particle, then it can be deduced from the spray equation (see Williams, ch.11, 1985), that the fluid phase was exposed to the force

$$M_\alpha = -\frac{\rho_p}{\rho_f} \frac{4\pi}{3} \int \int dr d\underline{v} r^3 F_\alpha^p f(r, \underline{x}, \underline{v}, t) \quad (27)$$

exerted by the particles. Here $f(r, \underline{x}, \underline{v}, t)$ was the probable number of particles in the radius range dr about r located in the spatial $d\underline{x}_\alpha$ range about x_α with particle velocities in the range $d\underline{v}_\alpha$ about v_α satisfying

$$N = \int dr \int d\underline{x} \int d\underline{v} f(r, \underline{x}, \underline{v}, t)$$

where N was the total number of particles in the domain of integration \mathcal{D} with volume $V > 0$. The solution $f(r, \underline{x}, \underline{v}, t)$ of the spray equation was in general not known and numerical simulation methods were applied to obtain the information on the force term (27). In a direct simulation method all particles would have been tracked individually and the distribution function $f(r, \underline{x}, \underline{v}, t)$ would be approximated by

$$\hat{f}(r, \underline{x}, \underline{v}, t) \equiv \sum_{i=1}^N \delta(r - r^i) \delta(\underline{x} - \underline{x}^i) \delta(\underline{v} - \underline{v}^i)$$

for a single realization and $f = \langle \hat{f} \rangle$ where the angular brackets indicate ensemble averaging. For the present numerical simulation a small subdomain \mathcal{D} (grid cell) was selected and the force M_α was integrated over it. It followed that

$$\frac{1}{V_c} \int_{\mathcal{D}} d\mathbf{x} M_\alpha = -\frac{\rho_p}{\rho_f} \sum_{i=1}^{N_c} \frac{V_i}{V_c} F_\alpha^i \quad (28)$$

holds, where the F^i were the forces on the N_c individual particles in the grid cell \mathcal{D} with volume V_c . The particle volumes were for spherical particles given by $V_i = \frac{4\pi}{3} r_i^3$. This force was then distributed among the grid points of the cell using Crowe's (1982) Particle-Source-In-Cell method.

The numerical simulations at the Reynolds number (10,000) of the experiments could not have resolved the complete range of scales present in the turbulent flow and the LES model described in section 1.1.1 was applied to simulate the effect of the unresolved part of the spectrum. Storage limitations did not allow the tracking of particles for mass loadings exceeding 5%. However, at this level of mass loading the dispersion produced by the LES simulation in Figure 7 showed clearly the phenomenon observed in the experiments. The location of the plateau in the dispersion curve was further downstream (at about $x/D \approx 10 - 13$) than in the experiment, but the shape was in good agreement with it. The explanation for this phenomenon can be found if the detailed flow structure in this region was considered. The particles were fed into the flow at the entrance section uniformly. Little change of the uniformity of the particle distribution over the cross section of the jet was observed for the first five diameters. Once the roll up of the ring vortices was completed and they started to interact the particles were transported laterally and the particle number density becomes increasingly non-uniform. At the location of the dispersion plateau seen in Figure 7 in the range $10 \leq x/D \leq 13$ a significant thinning of the particle distribution off the axis was observed. This indicated, that behind the first interaction region of the ring vortices (about $6 \leq x/D \leq 11$), which are generated by the Kelvin-Helmholtz instability of the cylindrical shear layer, a region exists, where the particles suffered acceleration in axial direction with significant lateral transport towards the jet axis. Inspection of the velocity field showed that this was indeed the case. The flow accelerated and moved towards the jet axis as indicated in the particle distribution. If several time instances were analyzed it became evident that the statistical result for the particle dispersion was the plateau in the dispersion emerging in Figure 7. Figure 8 showed two scatter plots of the numerically simulated distribution of the particles at the axial stations $x/D = 20$ and $x/D = 28$ downstream of the plateau region. The increase in variance of the particle displacement was clearly visible reflecting the expected increase of dispersion with axial distance.

The effect of the particles on the fluid phase as represented by the force M_α (28) in the momentum balance (18) was illustrated in Figure 9 to Figure 12. The contour lines of the θ -component of vorticity, which is responsible for lateral transport, was used to visualize the flow structure in the initial region of the jet. Figure 9 shows the case with particles injected at the entrance section and Figure 10 shows the flow under the same conditions without particle injection. It was seen that the presence of particles led to more ring vortices of smaller size generated in the initial region of the jet, than in the flow without particles.

The flow structures in the full computational region $1 \leq x/D \leq 30$ were presented as iso-lines of the axial and radial velocity components in Figure 11 without backscatter

effect (the term (28) was not included in the momentum balance) and Figure 12 with this effect. The reduction in scale was clearly visible but the backscatter effect was noticeably smaller in the downstream region. The presence of the particles induced a larger number of ring vortices, which were smaller and thus spaced more closely than in the flow without the backscatter effect.

1.1.3 Time integration schemes.

The second order accurate explicit Adams-Bashforth time integration scheme was known to be unstable for inviscid flows and thus not suitable for long time integration. It was, therefore, necessary to replace this scheme with schemes that were at least conditionally stable and at least as accurate. Several single and multi-step time integration schemes were analyzed (details can be found in the appendix) and two Runge-Kutta-type schemes were successfully tested. The fourth order Runge-Kutta scheme was described in detail in the appendix.

A standard third order Runge-Kutta method for an ode $y' = f(x, y)$ could be set up as follows

$$y^{n+1} = y^n + \gamma_0 k_0 + \gamma_1 k_1 + \gamma_2 k_2$$

where the increments were defined by

$$k_0 = \Delta t f(y^n)$$

$$k_1 = \Delta t f(y^n + \alpha_1 k_0)$$

$$k_2 = \Delta t f(y^n + \beta_{21} k_0 + \beta_{22} k_1)$$

and the constraints for the coefficients

$$\beta_{22} = \alpha_2 - \beta_{21}$$

$$\gamma_0 + \gamma_1 + \gamma_2 = 1$$

$$\gamma_1 \alpha_1 + \gamma_2 \alpha_2 = \frac{1}{2}$$

$$\gamma_1 \alpha_1^2 + \gamma_2 \alpha_2^2 = \frac{1}{3}$$

$$\gamma_2 \beta_{22} \alpha_1 = \frac{1}{6}$$

There was no unique set of constants and several variants of the third order method were available. The application of a Runge-Kutta time integration scheme to the solution of the Navier-Stokes equations in three dimensions introduced a new aspect to the construction of such a scheme: Minimization of storage requirements. A possible solution to the constraint equation was then given by

$$\alpha_1 = \frac{1}{2}, \quad \beta_{21} = \frac{1}{2}, \quad \beta_{22} = -\frac{1}{4}$$

$$\gamma_0 = \frac{2}{3}, \quad \gamma_1 = \frac{5}{3}, \quad \gamma_2 = -\frac{4}{3}$$

The procedure was tested for the solution of Burgers nonlinear second order pde with sixth order compact finite difference approximations for the convective and diffusive terms and the present third order Runge-Kutta time integration scheme. Absolute error bounds were established since the analytic solution for the periodic initial value problem was known

$$u(x, t) = \frac{2}{Re} \frac{M(x, t)}{N(x, t)}$$

where

$$\begin{aligned} M(x, t) &\equiv \sin(x) \exp\left(-\frac{t}{Re}\right) + \frac{1}{2} \sin(2x) \exp\left(-\frac{4t}{Re}\right) + \frac{3}{2} \sin(3x) \exp\left(-\frac{9t}{Re}\right) \\ &\quad + \frac{1}{2} \sin(4x) \exp\left(-\frac{16t}{Re}\right) + \frac{5}{8} \sin(5x) \exp\left(-\frac{25t}{Re}\right) \\ N(x, t) &\equiv 2 + \cos(x) \exp\left(-\frac{t}{Re}\right) + \frac{1}{4} \cos(2x) \exp\left(-\frac{4t}{Re}\right) + \frac{1}{2} \cos(3x) \exp\left(-\frac{9t}{Re}\right) \\ &\quad + \frac{1}{8} \cos(4x) \exp\left(-\frac{16t}{Re}\right) + \frac{1}{8} \cos(5x) \exp\left(-\frac{25t}{Re}\right) \end{aligned}$$

Restricting the time step by

$$\Delta t \leq Re \frac{\Delta x^2}{\pi^2}$$

the error was computed. Selecting $Re = 100$ and the time $t = 20$ the results were shown in Figure 13 and Figure 14 proving that the time integration was indeed third order and the spatial discretization was sixth order as claimed. The fourth order Runge-Kutta method for the Navier-Stokes equations was discussed in detail in the appendix.

The application of the Runge-Kutta methods to the Navier-Stokes equations was first carried out first for the case of two-dimensional flows in Cartesian and axi-symmetric coordinates in order to save CPU-time and speed up the testing. The case of third order Runge-Kutta time integration and compact spatial discretization to fourth order for the viscous terms and the pressure gradient and seventh order windward biased scheme for the convective terms applied to the axis-symmetric round jet was presented in Figure 15. The Reynolds number was $Re = 5000$ and the time $t = 46$ dimensionless units. The absolute value of vorticity was plotted for the first fifteen diameters of the jet. No disturbances were introduced and the natural instability of the axi-symmetric shear layer produces vortex roll-up and vortex merging. The maximum norm of vorticity in Figure 16 shows the variation with time due to the roll-up and merging processes. The check on mass balance was presented in Figure 17 in terms of the integral of the divergence of velocity as broken line (the exact value is zero) and the L_2 of the divergence. It was seen that both are satisfactory. The fourth order Runge-Kutta time integration method was implemented into the Cartesian version of the Navier-Stokes solver. Some results for two-dimensional flows were shown in Figure 18 and Figure 19. The vector plot for velocity for the plane jet in Figure 18 at the Reynolds number $Re = 2500$ and $t = 25$ indicated the difference between axi-symmetric and plane jets as the latter has a strong tendency to meander. The last test example was the backward facing step, which was simulated for the Reynolds number (based on the step height) $Re = 5000$ and the ratio of step height to channel width of one half. The flow was simulated starting with zero velocity and increasing the

inflow velocity to its steady state value in two time units. Two times were shown in Figure 19, $t = 15$ in the upper graph and $t = 25$ in the lower one. The flow was not yet fully developed as oscillating separating vortices dominate the flow. It was concluded from the results presented, that the Runge-Kutta time integration schemes were very promising for the full three-dimensional simulations. These schemes were implemented into the fully three-dimensional solver.

1.2 Experimental Approach.

The experimental method has built upon the pioneering work of Call and Kennedy (1991) wherein a method was developed and reported for the Lagrangian tracking of particles in a turbulent jet. Turbulent jets pose a particular problem for the description of particle dispersion in that the mean flow field undergoes a rapid change. Hence, unresponsive particles may find themselves lagging the development of the flow field. Although there have been a number of calculations of the dispersion of particles in turbulent jets with Lagrangian tracking methods, there have been few experimental studies of a Lagrangian nature. Call and Kennedy (1994) used the same experimental apparatus as the one that was used during this reporting period to investigate Lagrangian dispersion in a turbulent shear flow. Various sizes of vaporizing and non-vaporizing droplets were used. However, the experiments employed a limited range of particle and fluid time scales. The new experiments covered a wider range of time scales by variations in the particle size, the nozzle diameter and the jet exit velocity.

The experiment used hexadecane droplets that were more than 1000 droplet diameters apart. Consequently, there were no particle interactions. The particles were non vaporizing because the air was at room temperature (23°C) and the particles were measured in the flow for a relatively short time ($\ll 1\text{ s}$). Monodisperse droplets were produced by a piezo-electric crystal. The crystal was a hollow cylinder with a fuel inlet on one side and a nozzle on the other. A pulse generator supplied a pulse of variable voltage, frequency and width to the crystal. This voltage caused the crystal to contract and push a small amount of liquid through the nozzle. After the droplet was created, it was allowed to fall freely in the droplet shroud. The shroud ensured that the droplet remained on the centerline of the flow. The air was straightened through screens and a honeycomb before it came into contact with the droplet. The air and droplet were then accelerated through the converging nozzle and the droplet entered the jet on the centerline.

The droplet detection system used a He-Ne laser that crossed the centerline of the nozzle exit. As a droplet left the nozzle, it crossed the laser beam, scattering light that was focused onto a photo diode. This voltage signal was used to trigger the data collection system. Two laser sheets were formed by an argon-ion laser with associated optics. As the droplet passed through the sheets, a position sensitive photo multiplier tube detected the scattered light. The photomultiplier tube had four anode outputs whose magnitudes were proportional to the proximity of the centroid of the scattering image to the corresponding side of the detector. The signals were amplified before being digitized. At least 1000 droplets were measured in order to give statistically meaningful results. The position of a particle was determined from scattering from one laser sheet.

Measurement of the axial component of the particle velocity, u , required the use of two laser sheets. The distance between the center of the sheets was measured to give the length ΔL_u . The time between the peaks of scattering signals was calculated as follows.

Table 1. Particle Peclet Numbers for 60 μm Droplets $D = 7 \mu m$

$Re_j = 20,000$	$Re_j = 30,000$
39	43

 $D = 12.6 \mu m$

$Re_j = 20,000$	$Re_j = 30,000$
53	59

A Gaussian curve fit was applied to each signal with a linear regression performed on 31 data points. This process calculated the time of flight, Δt_u , between the sheets to $\Delta 1/4$ of one clock pulse. Hence, the axial velocity, u , was found from:

$$\frac{u(x_1) = \Delta L_u}{\Delta t_u}$$

In principle, the system should be capable of measuring the radial component of the droplet velocity. This component of velocity is more relevant to the radial dispersion than the axial velocity. However, it was found that in practice it was difficult to resolve accurately the rather small velocities in this direction with the present apparatus.

A TSI model 1053B hot wire anemometer was used for the velocity measurements of the air jet. The exit profiles for both the 7 mm and 12.6 mm nozzles exhibited a uniform exit velocity (top-hat) from both nozzles. The radial distance x_2 is normalized by the nozzle diameter D ; the velocity u , is normalized by the centerline exit velocity U_c .

The axial mean velocities and turbulence intensities within the air jet were also measured. It was apparent that the jet at a Reynolds number of 10,000 may not have been fully developed while the flow at the other Reynolds numbers appeared to exhibit the characteristics of high Reynolds number, self preserving turbulent flow. Measurements of the radial mean velocity profiles of the air at different axial positions (not shown) indicated that they were self-similar.

Measurements of particle statistics were obtained for a range of characteristic particle response times, nozzle diameters and jet exit velocities. It was found that increasing the Reynolds number of the jet by increasing the exit velocity resulted in less particle dispersion in the Eulerian frame as a result of the reduced response of the particles to the turbulence and the reduced time for a particle to travel from the nozzle exit to a given location downstream. Conversely, the particle dispersion in the Lagrangian frame i.e., as a function of time of flight, exhibited an increase with Reynolds number. Dispersion as a function of time of flight was quadratic for short times of flight. The function became linear for longer times. It was argued that when the local particle Stokes number was less than unity, the particle would behave like a fluid particle. The linear function was an indication of the plausibility of the assumption of Batchelor (1957) and of Monin and Yaglom (1979) that the Lagrangian statistics in a free shear flow would be self-preserving in the same manner as the Eulerian statistics. The Lagrangian Peclet numbers of the particles (shown in Table 1) approached the estimated value of the Eulerian Peclet number for a scalar in a round jet i. e., around 50. The results suggest that the calculation of particle dispersion in self-preserving flows such as jets can be simplified considerably once the local particle Stokes number is close to one. The simplification could be achieved by adopting

a constant particle diffusivity or equivalently, in the case of the round jet, by assuming that the dispersion of a given size class of particles increases linearly with time. Then the dispersion is equivalent to the variance of a Gaussian probability density function for particle location. Hence, the distribution of particles across the flow could be quite easily described as a function of the mean time of flight up to a given axial location. In that case, it would not be necessary to undertake the time consuming Monte Carlo sampling of a local probability distribution of gas phase velocities followed by solution of the particle equation of motion.

More details of these experiments may be found in the Appendix within the paper by Moody and Kennedy (submitted to Physics of Fluids, 1995).

1.2.1 Dispersion in a Spray.

Another major thrust of the experimental program during the lifetime of the grant was concerned with extending the measurements to particle dispersion in a turbulent spray. Fluorescent tagging was used to differentiate a particle from the surrounding droplets.

An ultrasonic atomizer was used to produce a fine spray with a SMD of around $50 \mu\text{m}$ (see Figure 21). The spray was introduced tangentially to the flow of air through a chamber (Figure 22). The chamber was designed to have a small flow of air through the walls and through the central tube to prevent the spray hitting the walls and creating drips. A considerable amount of work was necessary in order to achieve a design that permitted the spray to be introduced without dripping from the nozzle. Single droplets that were seeded with fluorescein dye were created at the top of the chamber with a piezoelectric droplet generator. The fluorescent droplet passed through the spray to leave the nozzle on the centerline. As it passed through an Argon ion laser sheet, it emitted fluorescence at a longer wavelength. The fluorescence was detected by a position sensing photomultiplier tube to yield a measure of the location and velocity of the particle.

A major challenge was to obtain good signals from the fluorescent particles in the very strong background Mie scattering from the spray. The background scattering was blocked with a Raman filter followed by a colored glass long pass filter. The combination of filters offered up to 6 orders of magnitude rejection of the laser wavelength.

It was demonstrated that it was possible to detect droplets as small as $30 \mu\text{m}$ against the scattering from a spray with a mass loading as high as 7%. The signal to noise ratio was excellent. It will be possible with this technique to determine the impact of the mass loading on the dispersion of the individual droplet a function of the time of flight and the droplet velocity. Higher mass loadings are required. Work is proceeding on improving our capability to form denser sprays.

Sprays with mass loadings from 0 up to 7% have been added to the jet. The signal to noise ratio under these conditions was about 110. The mean square displacement of the fluorescent droplet was measured at varying x/D from the exit of the nozzle. The dispersion is shown in Figure 7 for a pure air jet and for a spray with varying mass loadings. It was apparent that the spray contributes to the breakdown of the jet with larger spray loadings, resulting in greater dispersion of the tagged fluorescent droplets that were added to the flow. Another interesting feature of the results is the decrease in the dispersion at around $x/D \approx 8 - 10$.

1.3 References.

- Batchelor, G. K. (1957), "Diffusion in free turbulent shear flows", J. Fluid Mech. 3, 67.
- Boris, J.P. (1990), "Comments on subgrid turbulence models and large eddy simulations", in *Whither Turbulence? or Turbulence at the Crossroads* (J.L. Lumley ed.), Lecture Notes in Physics vol. 357, Springer V., 344
- Call, C.J. and Kennedy, I.M. (1991), "A technique for measuring Lagrangian and Eulerian particle statistics in a turbulent flow", Exper. in Fluids 12, 125.
- Call, C.J. and Kennedy, I.M. (1992), "Droplet dispersion, velocity and vaporization in heated and unheated jets", Paper No. 92-42 Spring Meeting of the Western States Section of the Combustion Institute, Corvallis OR, March 1992.
- Chorin, A.J. (1980), "Vortex models and boundary layer instability", SIAM J. Sci. Stat. Comput. 1, 1
- Crow, S.C. and Champagne, F.H. (1971), "Orderly structure in jet turbulence", J. Fluid Mechanics 48, 547
- Crowe, C.T., "Review - Numerical methods for dilute gas-particle flows", J. Fluids Engr., 104, 297-303, (1982).
- Dibble, R. W., Kollmann, W., Farshchi, M. and Schefer, R. W. (1986), "Second Order Closure for Turbulent Nonpremixed Flames: Scalar Dissipation and Heat Release Effects", *21st Symp. (Int.) Comb.*, The Comb. Inst., 1329
- Dukowicz, J.K., "A Particle-Fluid Numerical Model for Liquid Sprays", J. Comp. Physics, 35, 229-253, (1980).
- Eaton, J.K., "Experiments and simulations on turbulence modification by dispersed particles", Appl. Mech. Review, 47, S44-S48, (1994).
- Elghobashi, S.E. and Truesdell, G.C., "On the Interaction between Solid Particles and Decaying Turbulence", Eighth Symp. Turbulent Shear Flows, Munich, Germany, 731-736, (1991).
- Elghobashi, S.E. and Truesdell, G.C., "On the two-way interaction between homogeneous turbulence and dispersed solid particles I: Turbulence modification", Physics of Fluids A, 5, 1790-1801, (1993).
- Faeth, G.M. (1983), "Evaporation and combustion of sprays", Progr. Energy Comb. Sci. 9, 1
- Gore, R.A. and Crowe, C.T., "Effect of particle size on modulating turbulence intensity", Int. J. Multiphase Flow 15, 279 - 285 (1989).
- Grigorieff, R.D. (1977a), "Numerik gewöhnlicher Differentialgleichungen", vol.1, Teubner Studienbücher, Stuttgart.
- Grigorieff, R.D. (1977b), "Numerik gewöhnlicher Differentialgleichungen", vol.2, Teubner

Studienbücher, Stuttgart.

- Hansell, D., Kennedy, I.M. and Kollmann, W. (1992), "A simulation of particle dispersion in a turbulent jet", to appear in J. Multi-Phase Flow.
- Leonard, A. (1985), "Computing three-dimensional incompressible flows with vortex elements", Ann. Rev. Fluid Mech. **17**, 523
- Lundgren, T.S. and Ashurst, W.T. (1989), "Area-varying waves on curved vortex tubes with application to vortex breakdown", J. Fluid Mechanics **200**, 283
- Michalke, A. and Herrmann, G. (1982), "On the inviscid instability of a circular jet with external flow", J. Fluid Mechanics **114**, 343
- Monin, A.S. and Yaglom, A.M. (1979), *Statistical Fluid Mechanics: Mechanics of Turbulence*, (The MIT Press, Cambridge, MA).
- Moore, D.W. (1972), "Finite amplitude waves on aircraft trailing vortices", Aeronaut. Quart. **23**, 307
- Odar, F. and Hamilton, W.S. (1964), "Forces on a sphere accelerating in a viscous fluid", J. Fluid Mech. **18**, 302
- Putnam, A. (1961), "Integrable form of droplet drag coefficient", ARS J. **31**, 1467.
- Rai, M.M. and Moin, P. (1991), "Direct simulations of turbulent flow using finite-difference schemes", J. Comput. Physics **96**, 15
- Renksizbulut, M. and Yuen, M.C. (1983), "Experimental study of droplet evaporation in a high-temperature air stream", J. Heat Transfer **105**, 384
- Reynolds, W.C. (1990), "The potential and limitations of direct and large eddy simulations", in *Whither Turbulence? Turbulence at the Crossroads*, (J.L. Lumley ed.), Lecture Notes in Physics no. 357, Springer V., 313.
- Schlichting, H. (1960), "Boundary layer theory", 4th edition, McGraw Hill.
- Shuen, J.S., Solomon, A.S.P., Zhang, Q.F. and Faeth, G.M. (1985), "Structure of particle laden jets: Measurements and predictions", AIAA J. **23**, 396
- Snyder, W.K. and Lumley, J.L. (1971), "Some measurements of particle velocity autocorrelation functions in a turbulent flow", J. Fluid Mech. **48**, 41
- Solomon, A.S.P., Shuen, J.S., Zhang, Q.F. and Faeth, G.M. (1985), "Structure of non-evaporating sprays, part I: Initial conditions and mean properties", AIAA J. **23**, 1548
- Solomon, A.S.P., Shuen, J.S., Zhang, Q.F. and Faeth, G.M. (1985), "Structure of non-evaporating sprays, part II: Drop and turbulence properties", AIAA J. **23**, 1724
- Williams, F.A. (1985), "Combustion Theory", 2nd ed., Benjamin/Cummings Publ. Comp.
- Yule, A.J. (1978), "Large-scale structure in the mixing layer of a round jet", J. Fluid Mechanics **89**, 413

Yuu, S., Yasukouchi, N., Hirosawa, Y. and Jotaki, T. (1978), "Particle turbulent diffusion in a dust laden round jet", AIChE J., 24, 509

Appendix: Analysis of time integration schemes

Single step and multi-step time integration schemes were considered. Accuracy, stability, number of operations per step and storage requirements were the relevant properties for the application to the solution of the Navier-Stokes equations. The general theory for the numerical solution of systems of odes using single step methods were found in Grigorieff (1977a) and using multi-step methods in Grigorieff (1977b).

Adams-Basforth multi-step explicit schemes.

The ordinary differential equation

$$\frac{du}{dt} = f(t, u)$$

with the initial condition $u(0) = u_0$ was considered. Assuming that at least $m > 0$ steps have been computed, m values $u_{j+k} \equiv u(t_{j+k})$ and $f_{j+k} \equiv f(t_{j+k}, u_{j+k})$ for $k = 0, \dots, m-1$ were used to construct an explicit scheme for the calculation of u_{j+m} . The ode was integrated and the right side $f(t, u)$ was approximated by the interpolation polynomial $P(t)$ through the points $(t_j, f_j), \dots, (t_{j+m}, u_{j+m})$

$$u_{j+m} = u_{j+m-1} + \int_{t_{j+m-1}}^{t_{j+m}} dt' P(t')$$

The polynomial $P(t)$ was given by Newton's formula using backward differences as

$$P(t) = \sum_{k=0}^{m-1} (-1)^k \binom{-s}{k} \nabla^k f_{j+m-1}$$

where

$$s \equiv \frac{1}{h}(t' - t_{j+m-1})$$

and $\nabla^0 f_l = f_l$

$$\nabla^k f_l = \nabla^{k-1} f_l - \nabla^{k-1} f_{l-1}$$

The integration led to

$$u_{j+m} = u_{j+m-1} + \sum_{k=0}^{m-1} (-1)^k \nabla^k f_{j+m-1} \int_{t_{j+m-1}}^{t_{j+m}} dt' \binom{-s(t')}{k}$$

The integrals were evaluated and the result was the recursive relation

$$\gamma_k + \frac{1}{2}\gamma_{k-1} + \frac{1}{3}\gamma_{k-2} + \dots + \frac{1}{k+1}\gamma_0 = 1 \quad (18)$$

for $k = 0, 1, \dots, m-1$ and the scheme emerges in the form

$$u_{j+m} = u_{j+m-1} + h \sum_{k=0}^{m-1} \gamma_k \nabla^k f_{j+m-1} \quad (19)$$

The truncation error for this class of explicit schemes was given by $O(h^m)$. The special case $m = 2$ was the example important for the solution of the Navier-Stokes equations. This scheme was then regarded either as an explicit scheme or as predictor step of a PC-scheme. The coefficients γ_k were $\gamma_0 = 1$, $\gamma_1 = \frac{1}{2}$ and the scheme was given by

$$u_{j+2} = u_{j+1} + \frac{1}{2}h(3f_{j+1} - f_j) + O(h^2) \quad (20)$$

It requires three levels of the solution u_{j+2} , u_{j+1} and u_j . The scheme applied to the equation

$$\frac{\partial u}{\partial t} + c \frac{\partial u}{\partial x} = 0$$

can be shown (using the standard Fourier analysis) to be unconditionally unstable (Rai and Moin, 1991), but the instability sets in so slowly that it can be useful.

Adams-Moulton multi-step implicit schemes.

A modification of the Adams-Bashforth schemes leads to an implicit class of schemes. The values of u and f at the point t_{j+m} were added to the interpolation polynomial

$$P(t) = \sum_{k=0}^m (-1)^k \binom{-s}{k} \nabla^k f_{j+m}$$

with s defined now by

$$s \equiv \frac{t' - t_{j+m}}{h}$$

leading to

$$u_{j+m} = u_{j+m-1} + h \sum_{k=0}^m \nu_k \nabla^k f_{j+m} \quad (21)$$

with coefficients, determined by integration over the interpolating polynomial as for the Adams-Bashforth scheme, given by $\nu_0 = 1$ and

$$\nu_k + \frac{1}{2}\nu_{k-1} + \frac{1}{3}\nu_{k-2} + \cdots + \frac{1}{k+1}\nu_0 = 0 \quad (22)$$

for $k = 0, \dots, m$. The scheme was implicit since $f_{j+m} = f(t_{j+m}, u_{j+m})$ and its truncation error was given by $O(h^{m+1})$. The special case $m = 1$ was relevant to the solution of the Navier-Stokes equations. We obtained $\nu_0 = 1$ and $\nu_1 = -\frac{1}{2}$ and

$$u_{j+1} = u_j + \frac{1}{2}h(f_{j+1} + f_j) + O(h^2)$$

It required iteration to compute the solution u_{j+1} at the new time level.

Multi-step PC (predictor-corrector) schemes.

The explicit Adams-Bashforth and the implicit Adams-Moulton multi-step schemes can be combined into a system of predictor-corrector (PC) schemes. The general form of the PC schemes followed from (19) and (21)

$$u_{j+m} = u_{j+m-1} + h \sum_{k=0}^{m-1} \gamma_k \nabla^k f_{j+m-1} + O(h^m) \quad (23)$$

$$u_{j+m} = u_{j+m-1} + h \sum_{k=0}^m \nu_k \nabla^k f_{j+m} + O(h^{m+1}) \quad (24)$$

If the corrector step was adjusted to the same truncation error as the predictor step the scheme

$$u_{j+1}^* = u_j + h \sum_{k=0}^{m-1} \gamma_k \nabla^k f(t_j, u_j) \quad (23)$$

$$u_{j+1} = u_j + h \sum_{k=0}^{m-1} \nu_k \nabla^k f(t_{j+1}, u_{j+1}^*) \quad (24)$$

of order $O(h^m)$ emerged. The special case $m = 2$ with truncation error $O(h^2)$ is of particular importance and leads to the predictor step

$$u_{j+1}^* = u_j + \frac{1}{2}h[3f(t_j, u_j) - f(t_{j-1}, u_{j-1})] \quad (25)$$

and the corrector step

$$u_{j+1} = u_j + \frac{1}{2}h[f(t_{j+1}, u_{j+1}^*) + f(t_j, u_j)] \quad (26)$$

This scheme can be applied to the Navier-Stokes equations if the right side $f(t, u)$ was interpreted as the sum of convective, pressure gradient and viscous terms. The stability properties of the PC scheme (25), (26) were superior to the explicit Adams-Bashforth scheme (Grigorieff vol.2, 1977, section 2.10.4). The main disadvantages of multi-step schemes were the necessity to design a single step start-up scheme and the fact that the schemes discussed here were only valid for constant spacing in time.

Multi-step time integration schemes for the Navier-Stokes equations

The application of time integration schemes developed for systems of odes to the Navier-Stokes equations was not trivial since the incompressible equations (1) to (3) contained the mass balance which was not an evolution equation. The scheme (25), (26) was adapted to the Navier-Stokes equations. Denoting the spatial discretizations with $\frac{\delta^n}{\delta x^n}$ and $\frac{\delta^n}{\delta y^n}$, which will be specified later, the momentum balances (2) and (3) were given by

$$\frac{\partial u}{\partial t} = f_x(u, v, p, Re)$$

$$\frac{\partial v}{\partial t} = f_y(u, v, p, Re)$$

where

$$f_x(u, v, p, Re) \equiv -u \frac{\delta u}{\delta x} - v \frac{\delta u}{\delta y} - \frac{\delta p}{\delta x} + \frac{1}{Re} \left(\frac{\delta^2 u}{\delta x^2} + \frac{\delta^2 u}{\delta y^2} \right)$$

and

$$f_y(u, v, p, Re) \equiv -u \frac{\delta v}{\delta x} - v \frac{\delta v}{\delta y} - \frac{\delta p}{\delta y} + \frac{1}{Re} \left(\frac{\delta^2 v}{\delta x^2} + \frac{\delta^2 v}{\delta y^2} \right)$$

The predictor step consisted then of two operations, first the velocity is predicted according to (25, superscript refers to time level)

$$u^{*n+1} = u^n + \frac{1}{2} \Delta t [3f_x(u^n, v^n, p^n, Re) - f_x(u^{n-1}, v^{n-1}, p^{n-1}, Re)]$$

and

$$v^{*n+1} = v^n + \frac{1}{2} \Delta t [3f_y(u^n, v^n, p^n, Re) - f_y(u^{n-1}, v^{n-1}, p^{n-1}, Re)]$$

and second, the predicted velocity was then updated using mass balance. The velocity components u^{*n+1} , v^{*n+1} did not satisfy the discretized mass balance

$$\frac{\delta u^{*n+1}}{\delta x} + \frac{\delta v^{*n+1}}{\delta y} = D^{*n+1} \neq 0$$

The updated velocity components were required to satisfy mass balance, which is accomplished by

$$u'^{n+1} = u^{*n+1} - \frac{\delta}{\delta x} \Phi$$

$$v'^{n+1} = v^{*n+1} - \frac{\delta}{\delta y} \Phi$$

and

$$\frac{\delta u'^{n+1}}{\delta x} + \frac{\delta v'^{n+1}}{\delta y} = 0$$

leading to

$$\frac{\delta^2 \Phi}{\delta x^2} + \frac{\delta^2 \Phi}{\delta y^2} = -D^{*n+1}$$

The updated velocity components u'^{n+1}, v'^{n+1} must satisfy the momentum balances, which leads to the pressure correction

$$p'^{n+1} = p^n + \frac{3}{2} \frac{\Phi}{\Delta t}$$

This concluded the predictor step. It was important to note at this point, that the pressure correction method as described above only satisfies one of the two boundary conditions at fixed walls, namely the condition of no flow normal to the wall. The remaining no-slip condition can be enforced in the predictor step, where the momentum balances were solved for the primed velocity components. It must be tested whether this approach was suitable for highly unsteady flows around airfoils. Both no-slip conditions can be enforced in the pressure correction method at the expense of an additional Poisson equation.

The corrector step involves also two operations similar to the predictor step. The updated velocity and pressure enter the predictor step according to (26) as follows

$$u''^{n+1} = u^n + \frac{1}{2} \Delta t [f_x(u'^{n+1}, v'^{n+1}, p'^{n+1}, Re) + f_x(u^n, v^n, p^n, Re)]$$

$$v''^{n+1} = v^n + \frac{1}{2} \Delta t [f_y(u'^{n+1}, v'^{n+1}, p'^{n+1}, Re) + f_y(u^n, v^n, p^n, Re)]$$

The velocity components u''^{n+1}, v''^{n+1} and the pressure p'^{n+1} must be updated as for the predictor step to enforce the mass balance. Mass balance required

$$\frac{\delta u''^{n+1}}{\delta x} + \frac{\delta v''^{n+1}}{\delta y} = 0$$

Hence, the correction Φ^* was necessary

$$u^{n+1} = u''^{n+1} - \frac{\delta}{\delta x} \Phi^*$$

$$v^{n+1} = v''^{n+1} - \frac{\delta}{\delta y} \Phi^*$$

to insure it, which leads to

$$\frac{\delta^2 \Phi^*}{\delta x^2} + \frac{\delta^2 \Phi^*}{\delta y^2} = -D''^{n+1}$$

where D''^{n+1} denotes the divergence of u''^{n+1}, v''^{n+1} . The pressure associated with the updated velocity field can be determined as follows. Updated momentum balances given by

$$u^{n+1} = u^n + \frac{1}{2} \Delta t [f_x(u'^{n+1}, v'^{n+1}, p'^{n+1} + p_c, Re) + f_x(u^n, v^n, p^n, Re)]$$

and

$$v^{n+1} = v^n + \frac{1}{2} \Delta t [f_y(u'^{n+1}, v'^{n+1}, p'^{n+1} + p_c, Re) + f_y(u^n, v^n, p^n, Re)]$$

were used to compute the pressure correction p_c . Subtracting the corrector step momentum balance from the updated versions led to

$$p_c = \frac{2\Phi^*}{\Delta t}$$

and the updated pressure was then given by

$$p^{n+1} = p'^{n+1} + p_c$$

It was clear that both corrector and predictor steps required updating to satisfy mass balance. The question remains how the stability of this type of scheme is modified by the updating steps.

Runge-Kutta explicit schemes

The family of Runge-Kutta schemes can be applied to the unsteady Navier-Stokes equations, if proper care was taken of mass balance. The momentum balances were written as in the previous section as

$$\begin{aligned}\frac{\partial u}{\partial t} &= f_x(u, v, p, Re) \\ \frac{\partial v}{\partial t} &= f_y(u, v, p, Re)\end{aligned}$$

together with mass balance

$$u_x + v_y = 0$$

The standard fourth order accurate Runge-Kutta method was considered for this system of equations. The solution at the new time level was constructed as the linear combination of four increments. Mass balance must be satisfied at the new time level, which can be insured by requiring it for each of the increments. The increments were then computed as follows.

Step (1): The increments $k_1(u)$ and $k_1(v)$ were computed using the momentum balances and then modified to enforce mass balance. The momentum balances produce the increments $\hat{k}_1(u)$ and $\hat{k}_1(v)$

$$\hat{k}_1(u) = \Delta t f_x(u^n, v^n, p^n, Re)$$

$$\hat{k}_1(v) = \Delta t f_y(u^n, v^n, p^n, Re)$$

which did not satisfy mass balance

$$\frac{\delta}{\delta x} \hat{k}_1(u) + \frac{\delta}{\delta y} \hat{k}_1(v) = D^{(1)} \neq 0$$

The correction potential $\Phi^{(1)}$ was required to correct the velocity increments

$$k_1(u) = \hat{k}_1(u) - \frac{\delta}{\delta x} \Phi^{(1)}$$

$$k_1(v) = \hat{k}_1(v) - \frac{\delta}{\delta y} \Phi^{(1)}$$

It was determined by enforcing mass balance for the corrected increments, which led to

$$\left(\frac{\delta^2}{\delta x^2} + \frac{\delta^2}{\delta y^2} \right) \Phi^{(1)} = -D^{(1)}$$

The pressure correction was then obtained from the requirement that the corrected increments satisfy the momentum balances

$$k_1(u) = \Delta t f_x(u^n, v^n, p^n + p_c^{(1)}, Re)$$

$$k_1(v) = \Delta t f_y(u^n, v^n, p^n + p_c^{(1)}, Re)$$

leading to

$$p_c^{(1)} = \frac{\rho \Phi^{(1)}}{\Delta t}$$

The increments for the velocity components and the pressure were thus computed.

Step (2): The increments $\hat{k}_2(u)$ and $\hat{k}_2(v)$ were computed using the momentum balances and then modified as in step (1). The increments

$$\hat{k}_2(u) = \Delta t f_x(u^n + \frac{1}{2}k_1(u), v^n + \frac{1}{2}k_1(v), p^n + \frac{1}{2}p_c^{(1)}, Re)$$

$$\hat{k}_2(v) = \Delta t f_y(u^n + \frac{1}{2}k_1(u), v^n + \frac{1}{2}k_1(v), p^n + \frac{1}{2}p_c^{(1)}, Re)$$

did not satisfy mass balance

$$\frac{\delta}{\delta x} \hat{k}_2(u) + \frac{\delta}{\delta y} \hat{k}_2(v) = D^{(2)} \neq 0$$

and the correction potential $\Phi^{(2)}$ was required as before

$$k_2(u) = \hat{k}_2(u) - \frac{\delta}{\delta x} \Phi^{(2)}$$

$$k_2(v) = \hat{k}_2(v) - \frac{\delta}{\delta y} \Phi^{(2)}$$

It was determined by

$$(\frac{\delta^2}{\delta x^2} + \frac{\delta^2}{\delta y^2}) \Phi^{(2)} = -D^{(2)}$$

The pressure correction was then obtained from the requirement that the corrected increments satisfy the momentum balances

$$k_2(u) = \Delta t f_x(u^n + \frac{1}{2}k_1(u), v^n + \frac{1}{2}k_1(v), p^n + p_c^{(2)}, Re)$$

$$k_2(v) = \Delta t f_y(u^n + \frac{1}{2}k_1(u), v^n + \frac{1}{2}k_1(v), p^n + p_c^{(2)}, Re)$$

leading to

$$p_c^{(2)} = \frac{\rho \Phi^{(2)}}{\Delta t}$$

The increments for the velocity components and the pressure were thus computed.

Step (3): The increments $\hat{k}_3(u)$ and $\hat{k}_3(v)$ were computed using the momentum balances and then modified as in step (2). The increments

$$\hat{k}_3(u) = \Delta t f_x(u^n + \frac{1}{2}k_2(u), v^n + \frac{1}{2}k_2(v), p^n + \frac{1}{2}p_c^{(2)}, Re)$$

$$\hat{k}_3(v) = \Delta t f_y(u^n + \frac{1}{2}k_2(u), v^n + \frac{1}{2}k_2(v), p^n + \frac{1}{2}p_c^{(2)}, Re)$$

did not satisfy mass balance

$$\frac{\delta}{\delta x} \hat{k}_3(u) + \frac{\delta}{\delta y} \hat{k}_3(v) = D^{(3)} \neq 0$$

and the correction potential $\Phi^{(3)}$ was required as before

$$k_3(u) = \hat{k}_3(u) - \frac{\delta}{\delta x} \Phi^{(3)}$$

$$k_3(v) = \hat{k}_3(v) - \frac{\delta}{\delta y} \Phi^{(3)}$$

It was determined by

$$(\frac{\delta^2}{\delta x^2} + \frac{\delta^2}{\delta y^2}) \Phi^{(3)} = -D^{(3)}$$

The pressure correction was then obtained from the requirement that the corrected increments satisfied the momentum balances

$$k_3(u) = \Delta t f_x(u^n + \frac{1}{2}k_2(u), v^n + \frac{1}{2}k_2(v), p^n + p_c^{(3)}, Re)$$

$$k_3(v) = \Delta t f_y(u^n + \frac{1}{2}k_2(u), v^n + \frac{1}{2}k_2(v), p^n + p_c^{(3)}, Re)$$

leading to

$$p_c^{(3)} = \frac{\rho \Phi^{(3)}}{\Delta t}$$

The increments for the velocity components and the pressure were thus computed.

Step (4): The increments $\hat{k}_4(u)$ and $\hat{k}_4(v)$ were computed using the momentum balances and then modified as in step (3). The increments

$$\hat{k}_4(u) = \Delta t f_x(u^n + k_3(u), v^n + k_3(v), p^n + p_c^{(3)}, Re)$$

$$\hat{k}_4(v) = \Delta t f_y(u^n + k_3(u), v^n + k_3(v), p^n + p_c^{(3)}, Re)$$

did not satisfy mass balance

$$\frac{\delta}{\delta x} \hat{k}_4(u) + \frac{\delta}{\delta y} \hat{k}_4(v) = D^{(4)} \neq 0$$

and the correction potential $\Phi^{(4)}$ was required as before

$$k_4(u) = \hat{k}_4(u) - \frac{\delta}{\delta x} \Phi^{(4)}$$

$$k_4(v) = \hat{k}_4(v) - \frac{\delta}{\delta y} \Phi^{(4)}$$

It was determined by

$$\left(\frac{\delta^2}{\delta x^2} + \frac{\delta^2}{\delta y^2} \right) \Phi^{(4)} = -D^{(4)}$$

The pressure correction was then obtained from the requirement that the corrected increments satisfy the momentum balances

$$k_4(u) = \Delta t f_x(u^n + k_3(u), v^n + k_3(v), p^n + p_c^{(4)}, Re)$$

$$k_4(v) = \Delta t f_y(u^n + k_3(u), v^n + k_3(v), p^n + p_c^{(4)}, Re)$$

leading to

$$p_c^{(4)} = \frac{\rho \Phi^{(4)}}{\Delta t}$$

The increment computation was thus completed.

The velocity and pressure at the new time level were then given by

$$u^{n+1} = u^n + \frac{1}{6}(k_1(u) + 2k_2(u) + 2k_3(u) + k_4(u))$$

$$v^{n+1} = v^n + \frac{1}{6}(k_1(v) + 2k_2(v) + 2k_3(v) + k_4(v))$$

$$p^{n+1} = p^n + \frac{1}{6}(p_c^{(1)} + 2p_c^{(2)} + 2p_c^{(3)} + p_c^{(4)})$$

according to the standard Runge-Kutta method. The new velocity field clearly satisfies mass balance since all increments do. The new pressure could be computed as $p^{n+1} = p^n + p_c^{(4)}$ or as linear combination of the pressure corrections associated with the individual velocity increments. The forth order Runge-Kutta method allows easy control of the time step according to

$$\kappa_{min} \leq 2 \frac{\|k_3(u) - k_2(u)\|}{\|k_2(u) - k_1(u)\|} \leq \kappa_{max}$$

and

$$\kappa_{min} \leq 2 \frac{\|k_3(v) - k_2(v)\|}{\|k_2(v) - k_1(v)\|} \leq \kappa_{max}$$

where the maximum norm was used for the velocity increments. The strategy for the time step control was then to double the time step if both ratios were below $\kappa_{min} = 0.01$ and to half the time step if one of the two ratios was above $\kappa_{max} = 0.05$.

VORTICITY MAGNITUDE
60 D UNLV Run
18 D in Radius

MACH
ALPHA
Re
TIME
GRID
0.071
0.00 DEG
 7.50×10^{-3}
 8.98×10^{-2}
 $62 \times 16 \times 190$



Figure 1: LES simulation of a turbulent round jet at $Re = 15,000$ without SGS model
 $c_s = 0.0$: Vorticity magnitude at time $t = 898$.

VORTICITY MAGNITUDE
60 D UNLV LES run
 $c_s = 0.025$, 18 D in radius

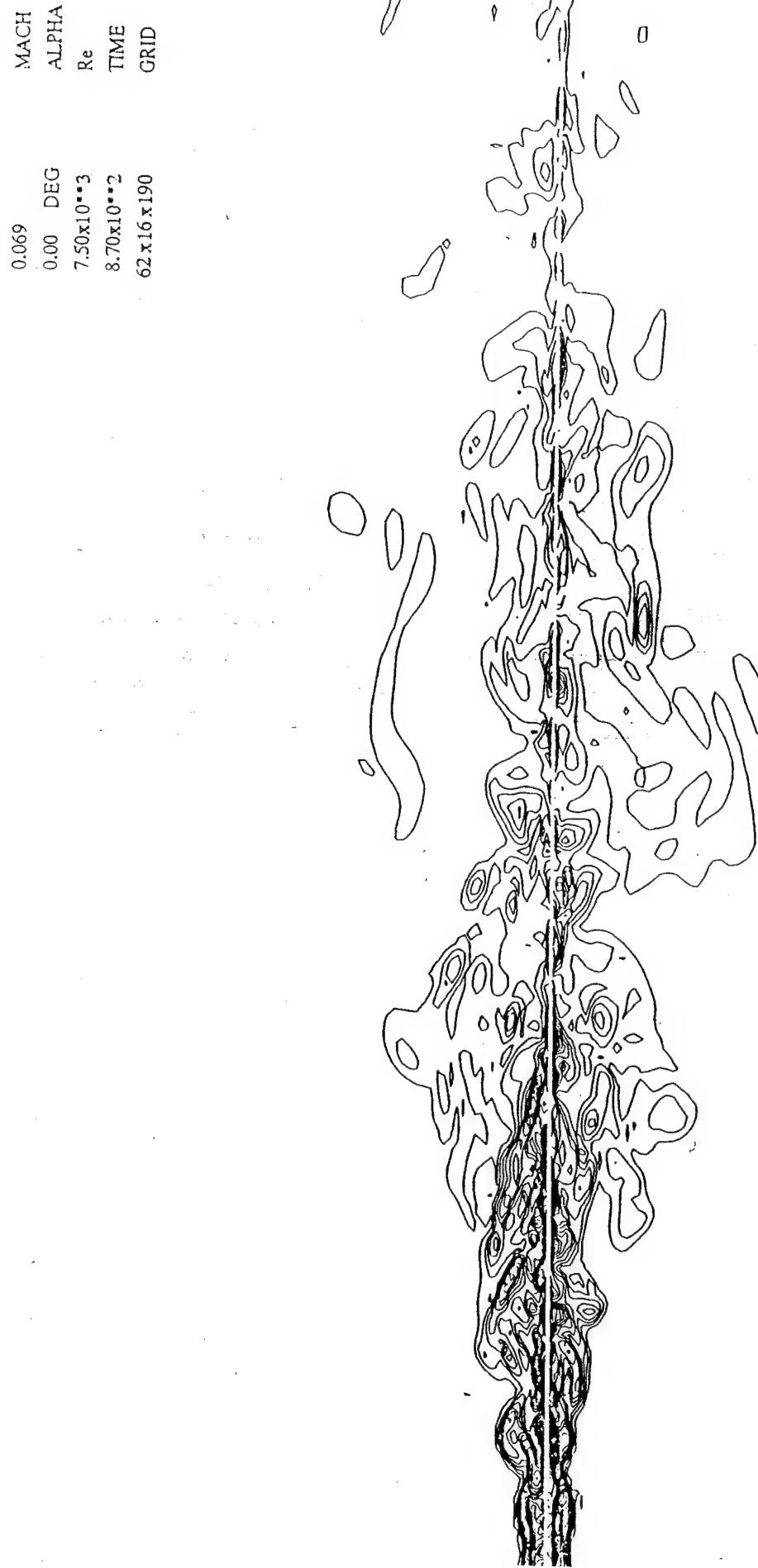


Figure 2: Simulation as in figure 1 with SGS model: $c_s = 0.025$.

113 μM vap. Pentane, 60° Heated Jet, $T_i=305$, $C_s=.05$, $Sch=1.$

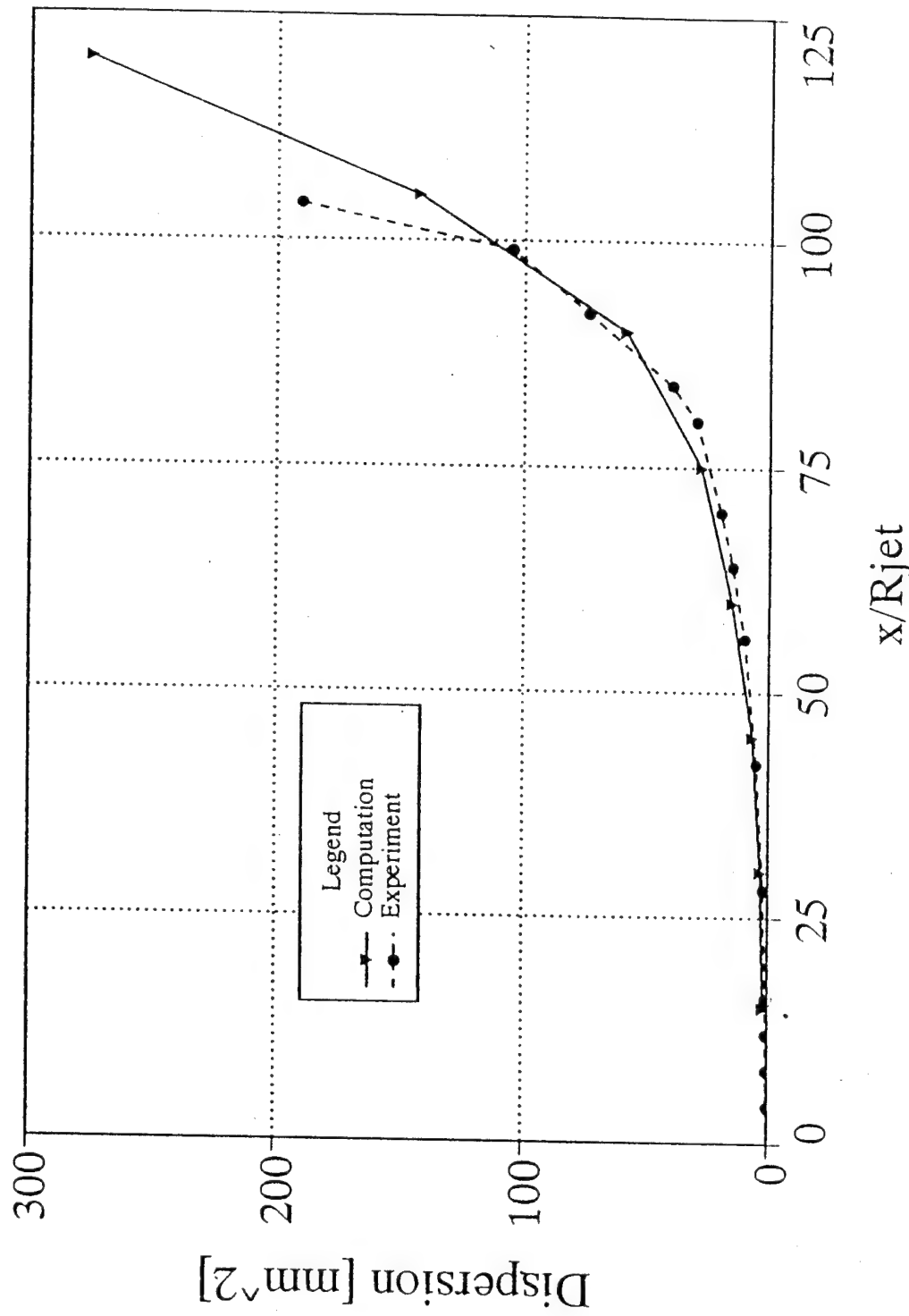


Figure 3: Spatial dispersion of $113 \mu\text{m}$ vaporizing Pentane droplets in a heated turbulent round jet (entrance temperature $T_i = 305^\circ\text{K}$, LES simulation with $c_s = 0.05$, $S_c = 1.0$).

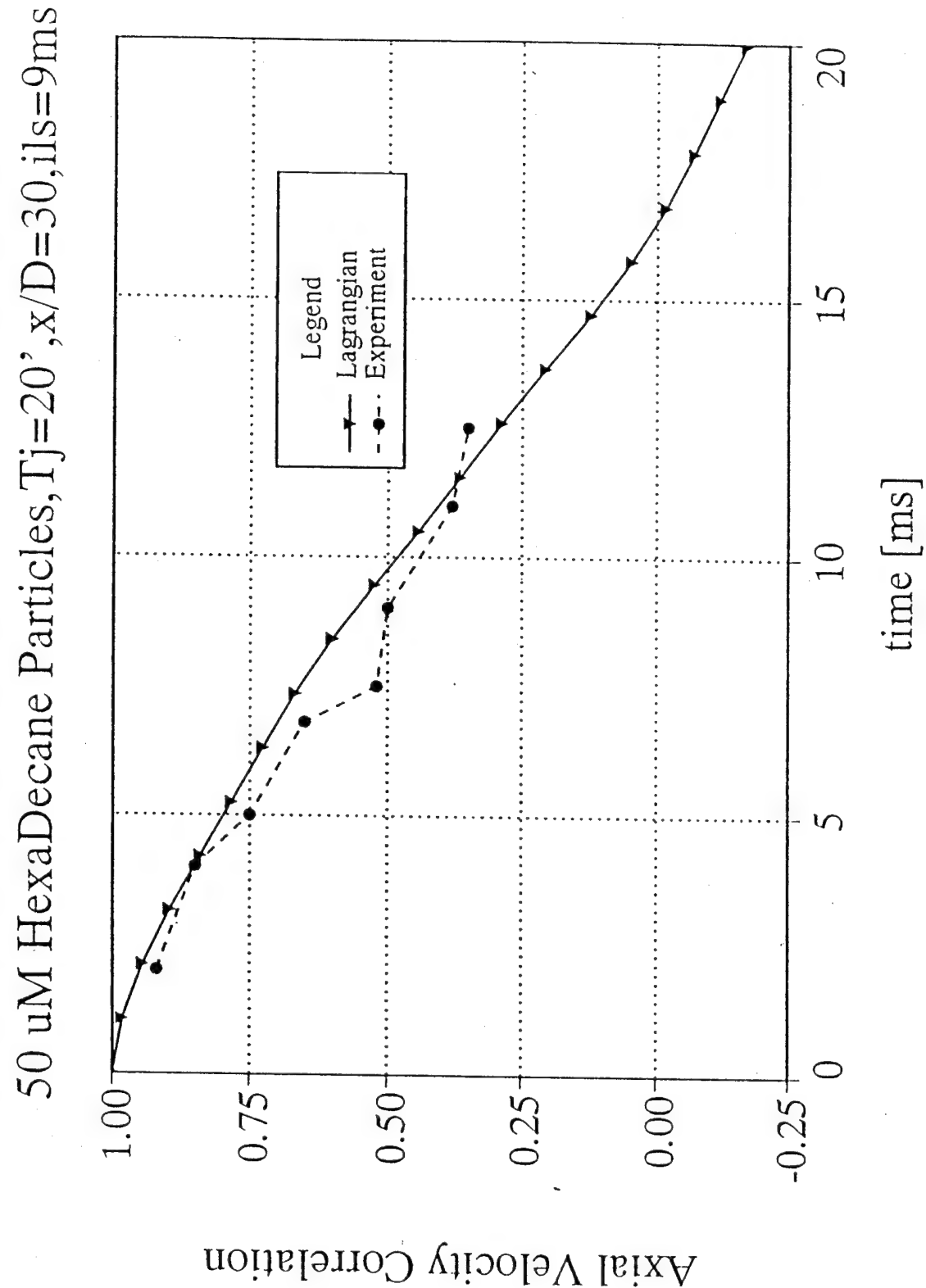


Figure 4: Axial velocity auto-correlation function for $50 \mu\text{m}$ Hexadecane droplets.

113 μM vap. C₅H₁₂, 60° Heated Jet, $T_i=305$, $C_s=.05$, $Sch=1.5$

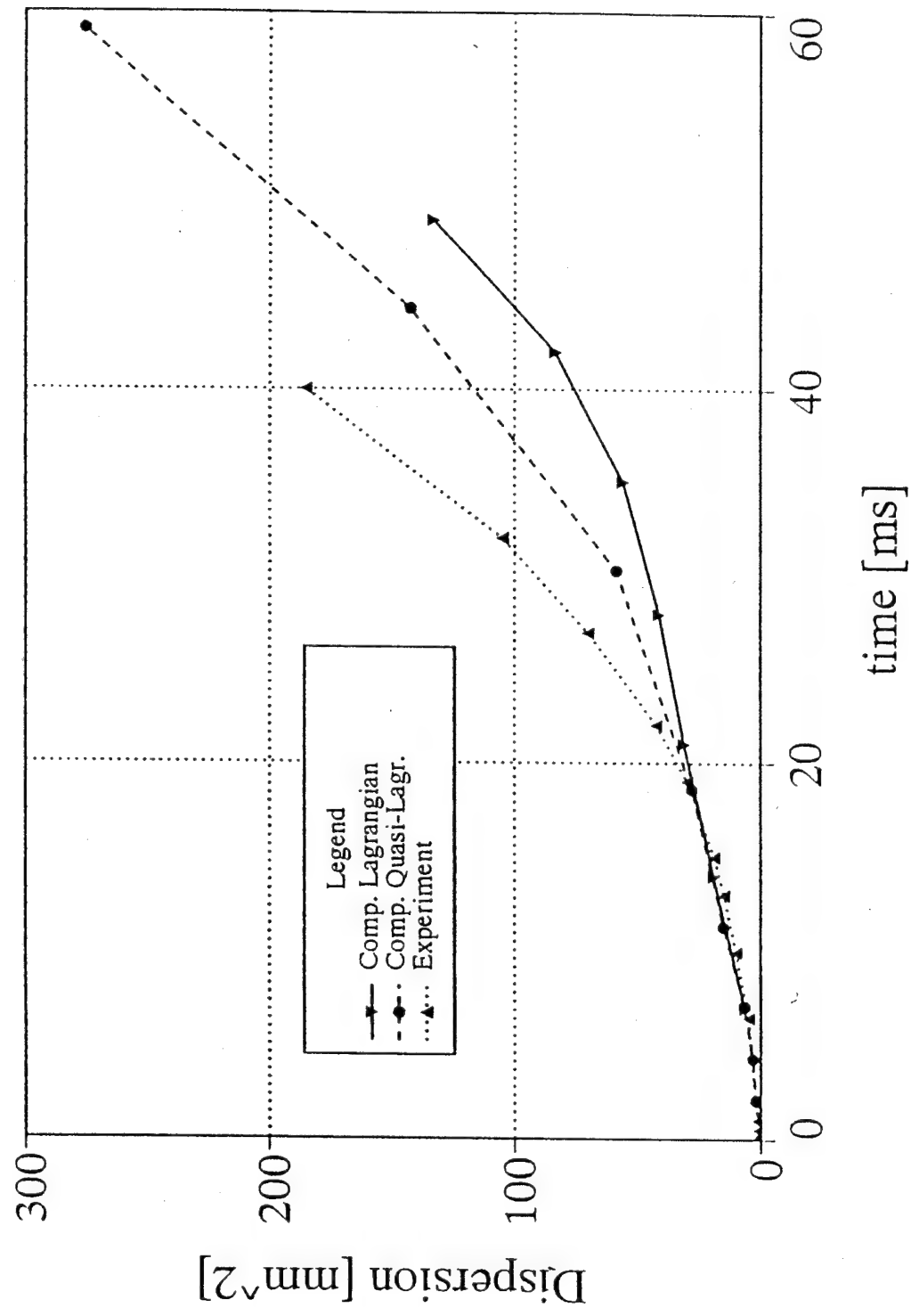


Figure 5: Temporal dispersion of 113 μm vaporizing C₅H₁₂ droplets in a heated turbulent round jet (entrance temperature $T_i = 305^\circ\text{K}$, LES simulation with $c_s = 0.05$, $Sch = 1.5$).

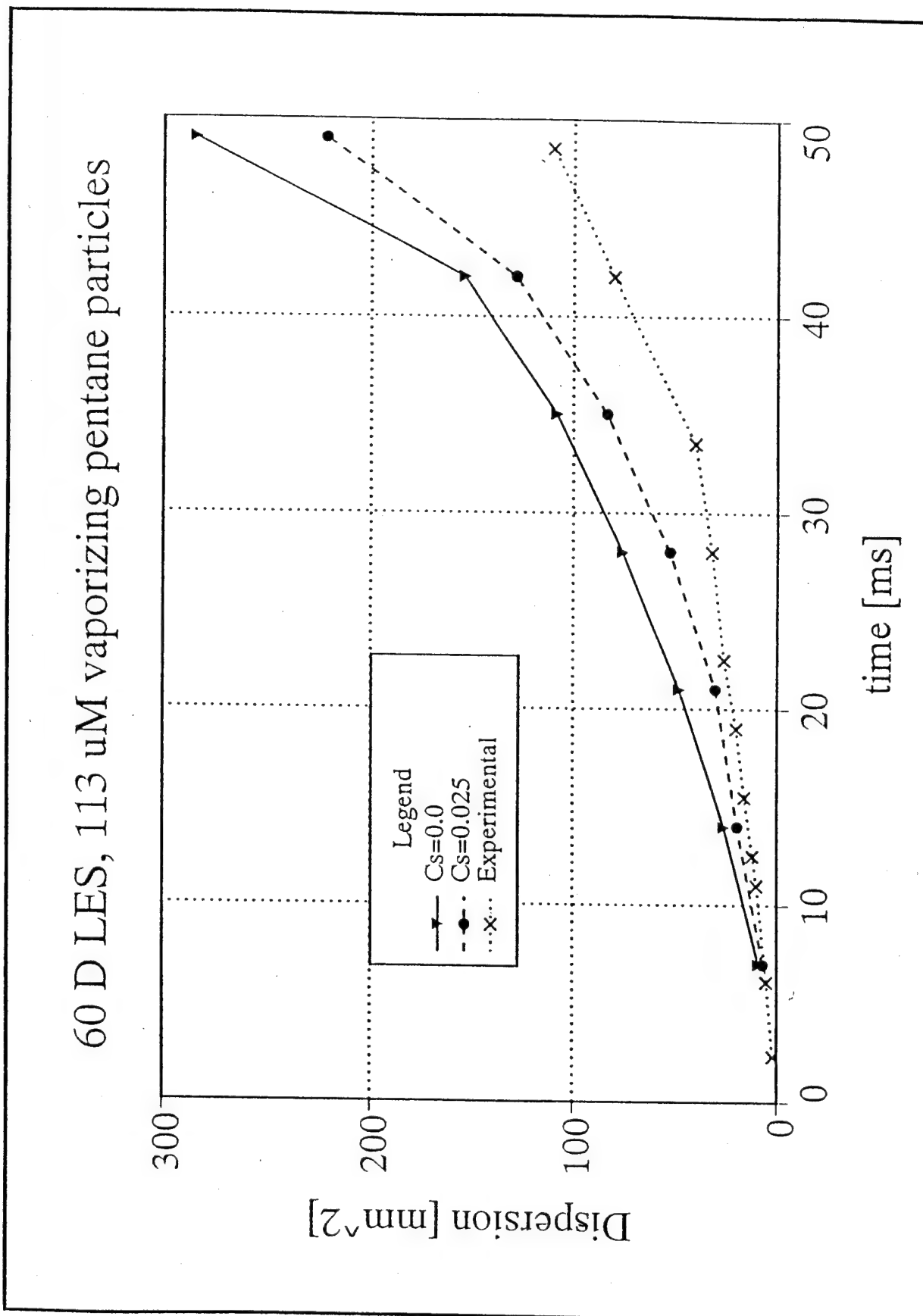


Figure 6: Same as figure 5 with two values for the Smagorinsky constant.

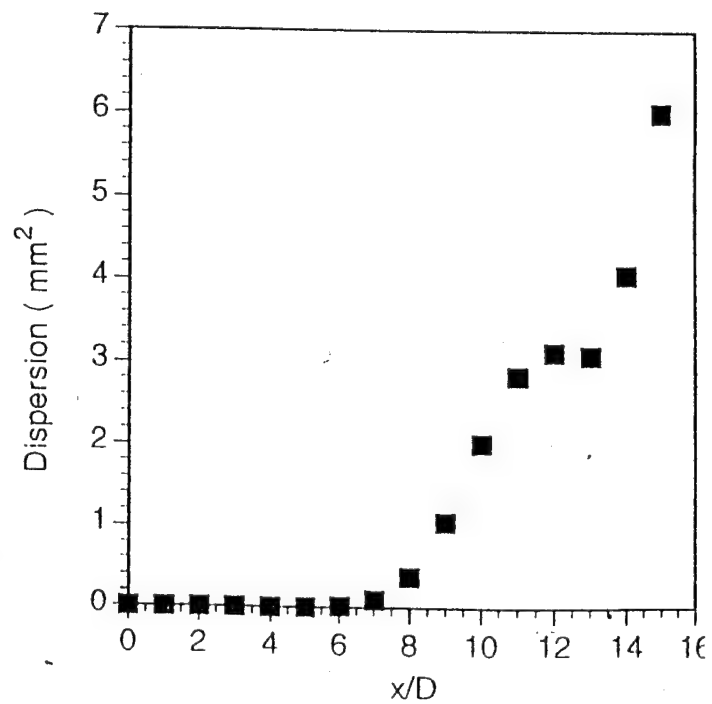
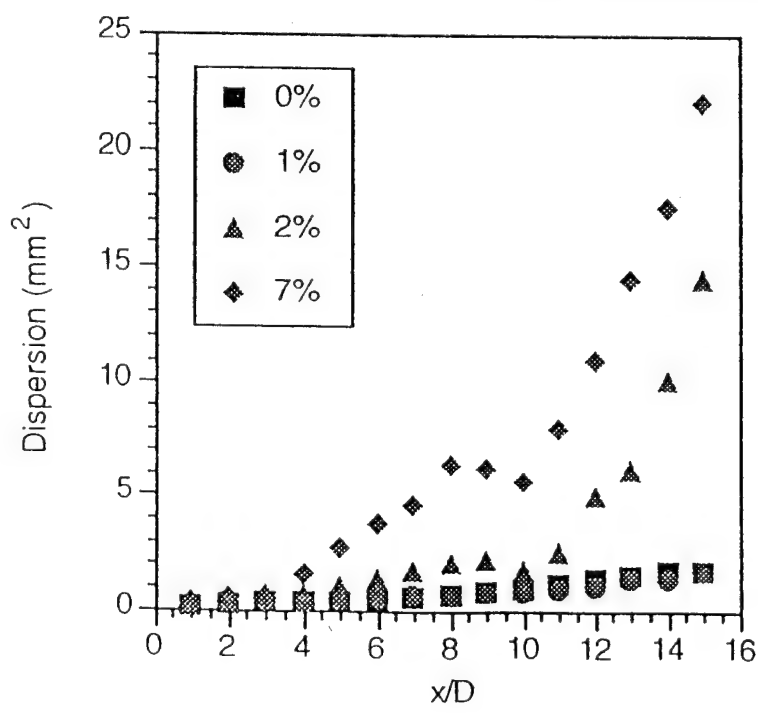
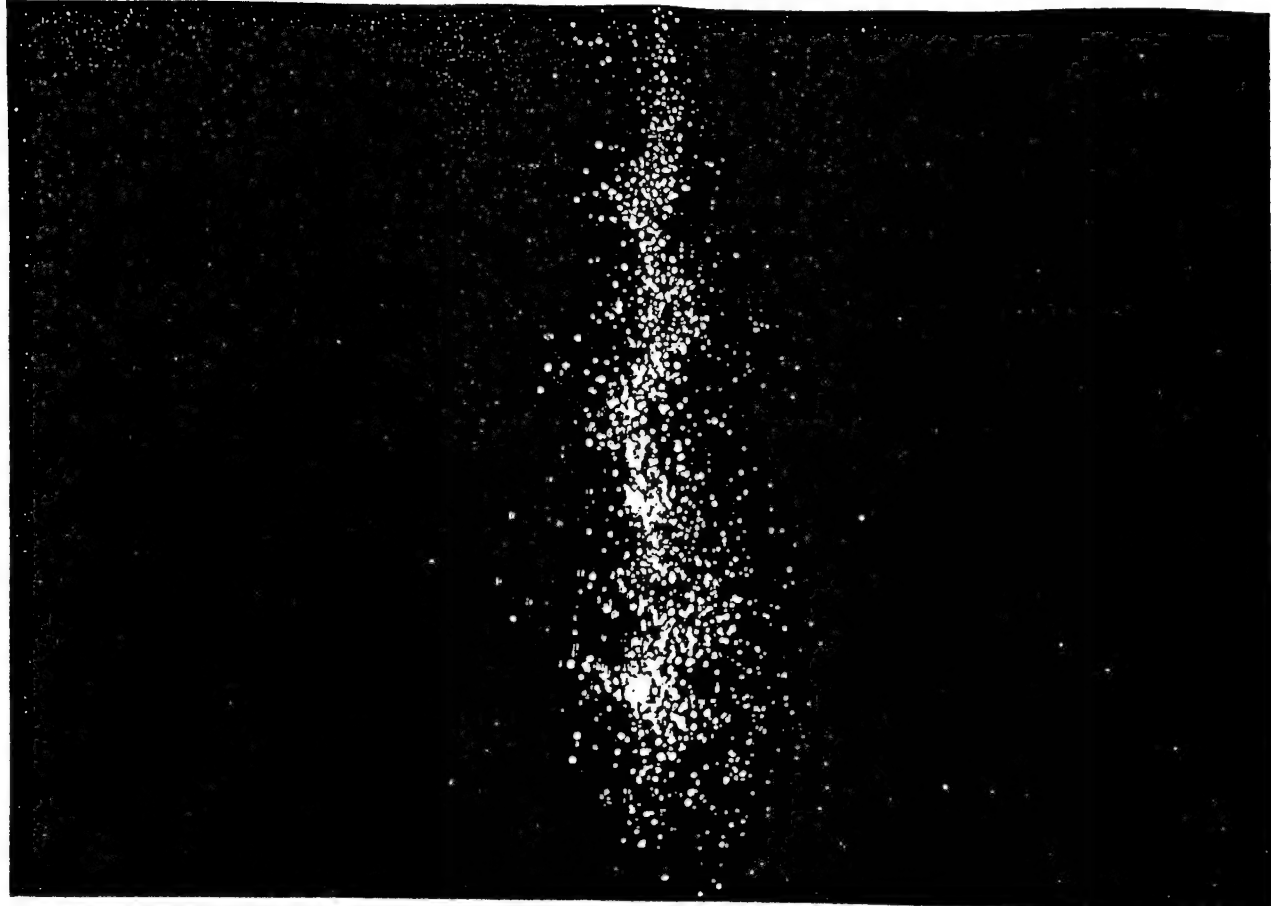


Figure 7: Dispersion of water droplets in a particle laden turbulent round jet for different mass loadings (experiments: left graph) and the mass loading 5% (LES simulation: right graph). Top: Photo of Spray.

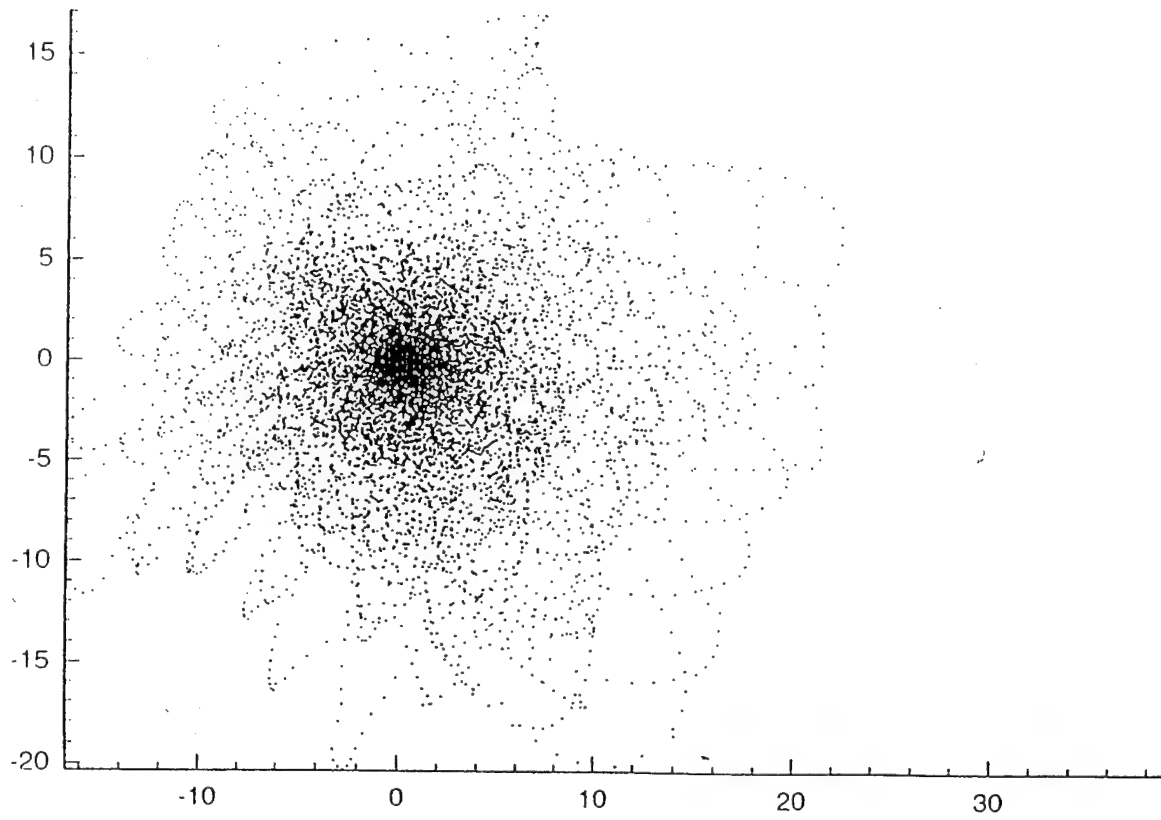
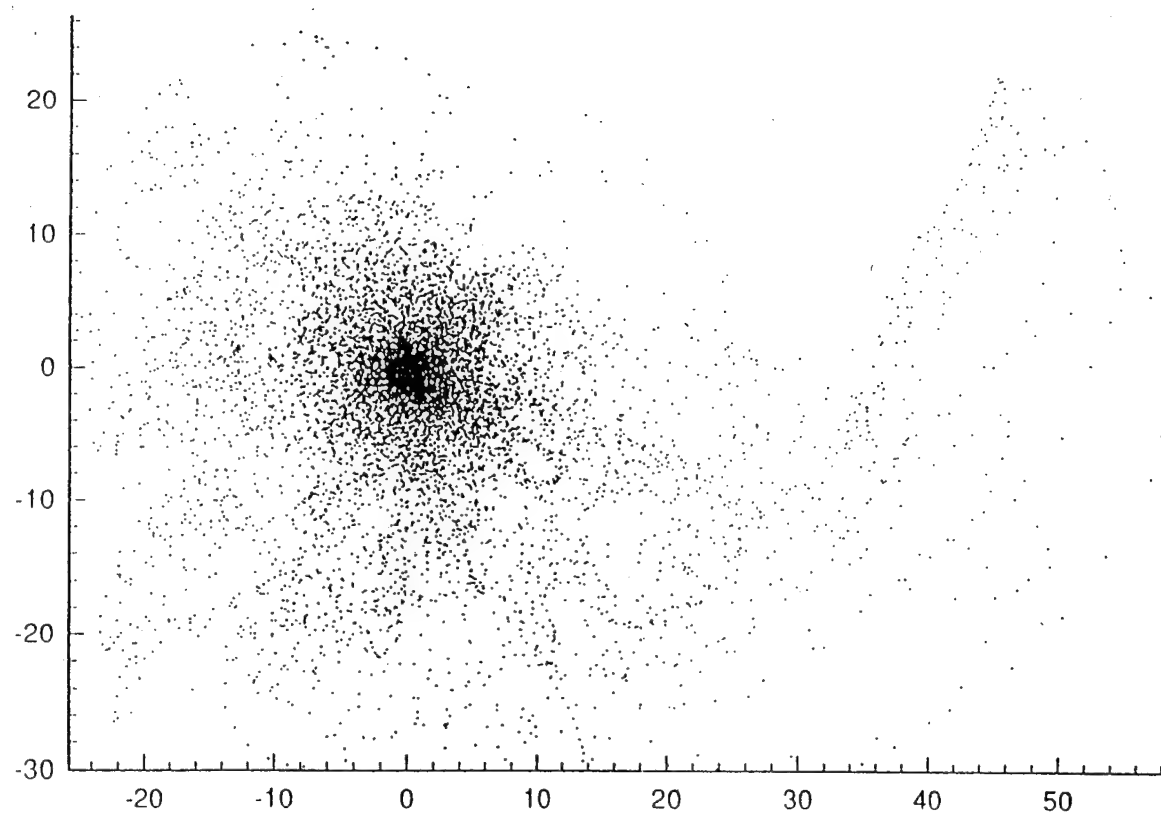


Figure 8: Scatter plot of particle locations at $x/D = 20$ (lower graph) and at $x/D = 28$ (upper graph) obtained with an LES simulation at $Re = 13,000$.

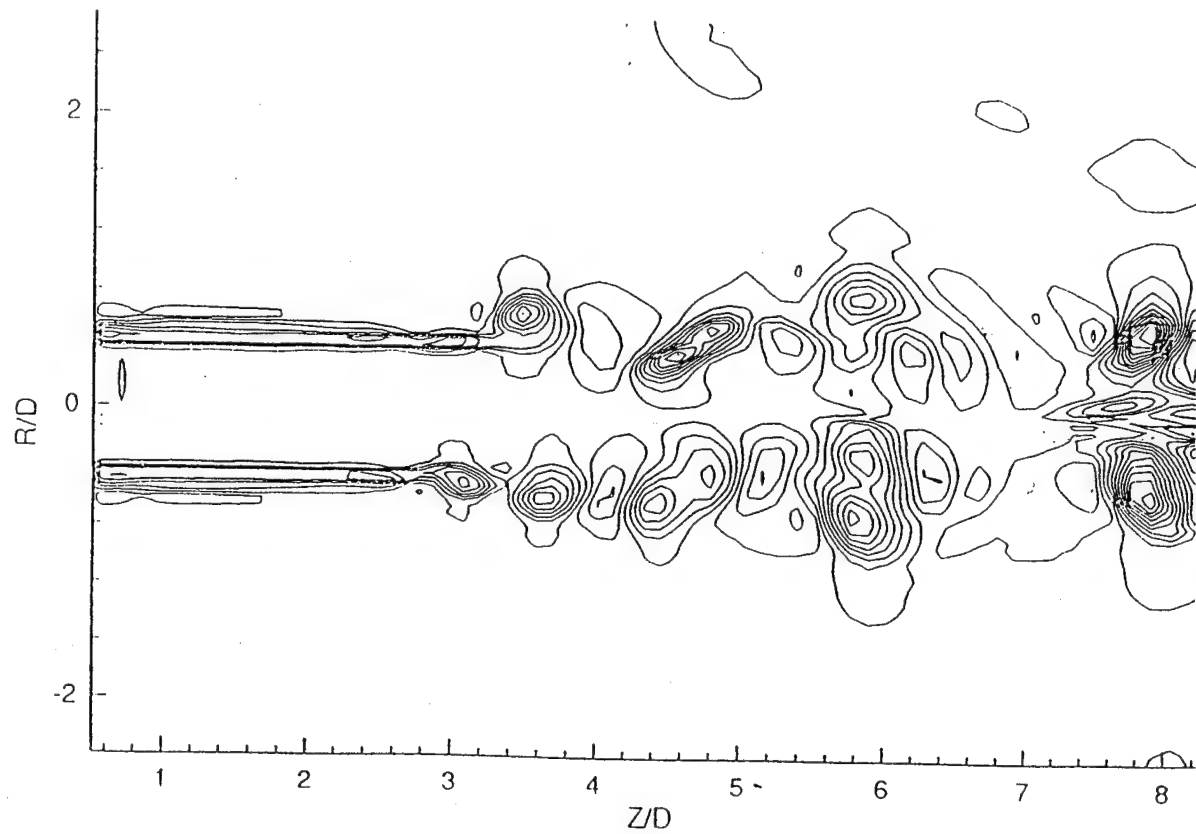
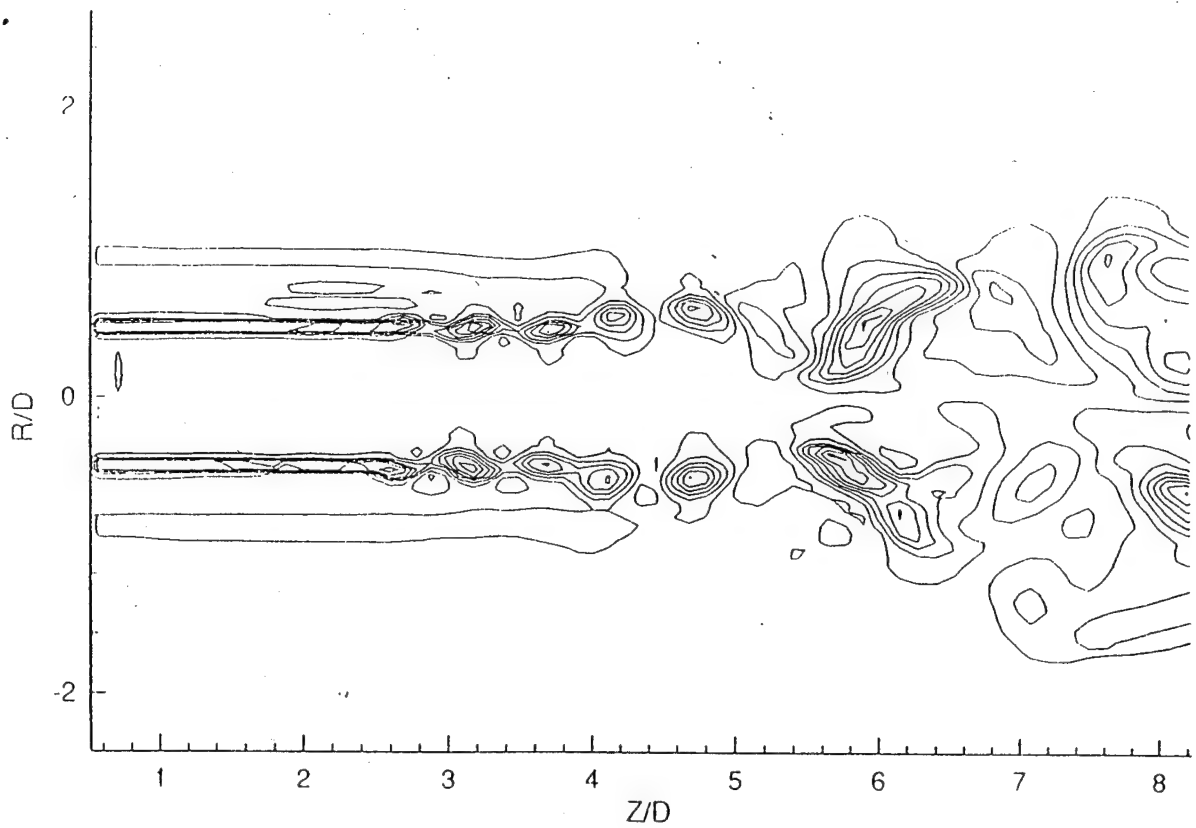


Figure 9: Computed iso-lines of the θ -component of vorticity in the initial region of an air jet with 5% mass loading (upper graph) and without spray (lower graph).

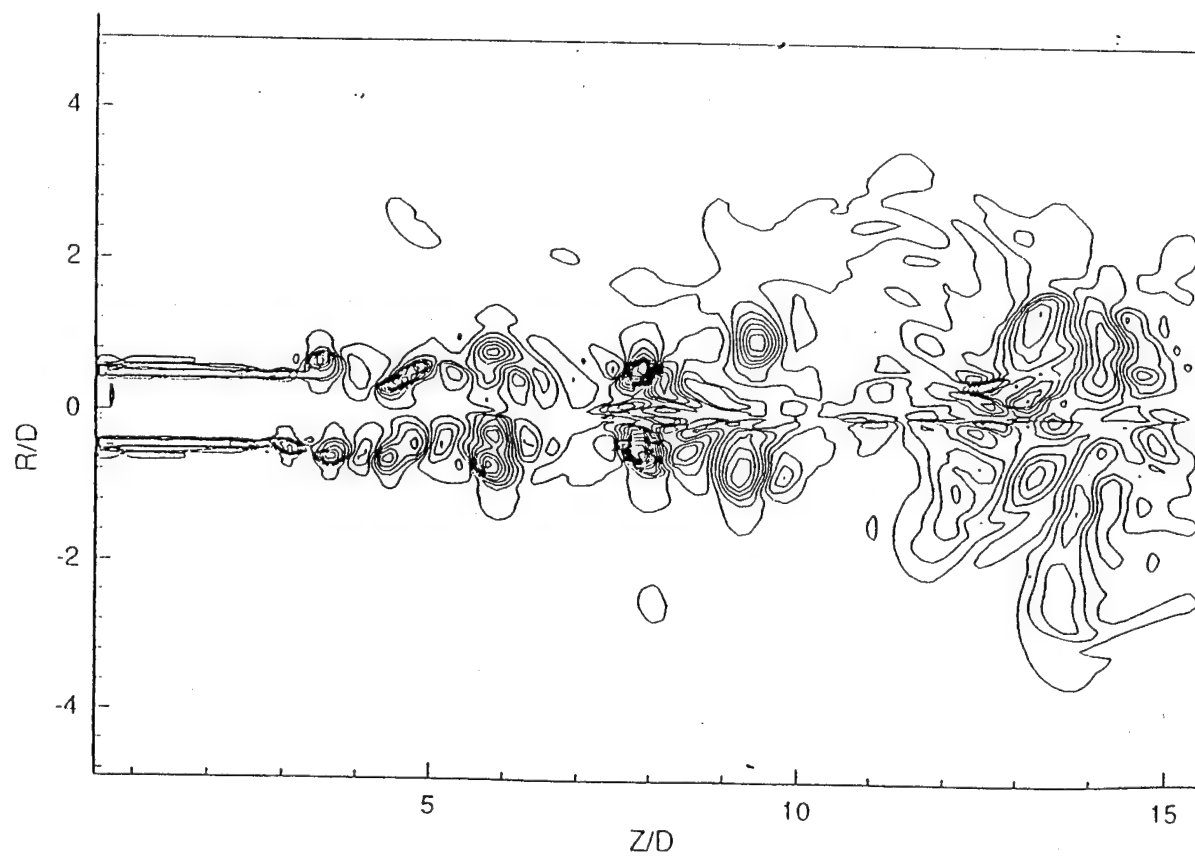
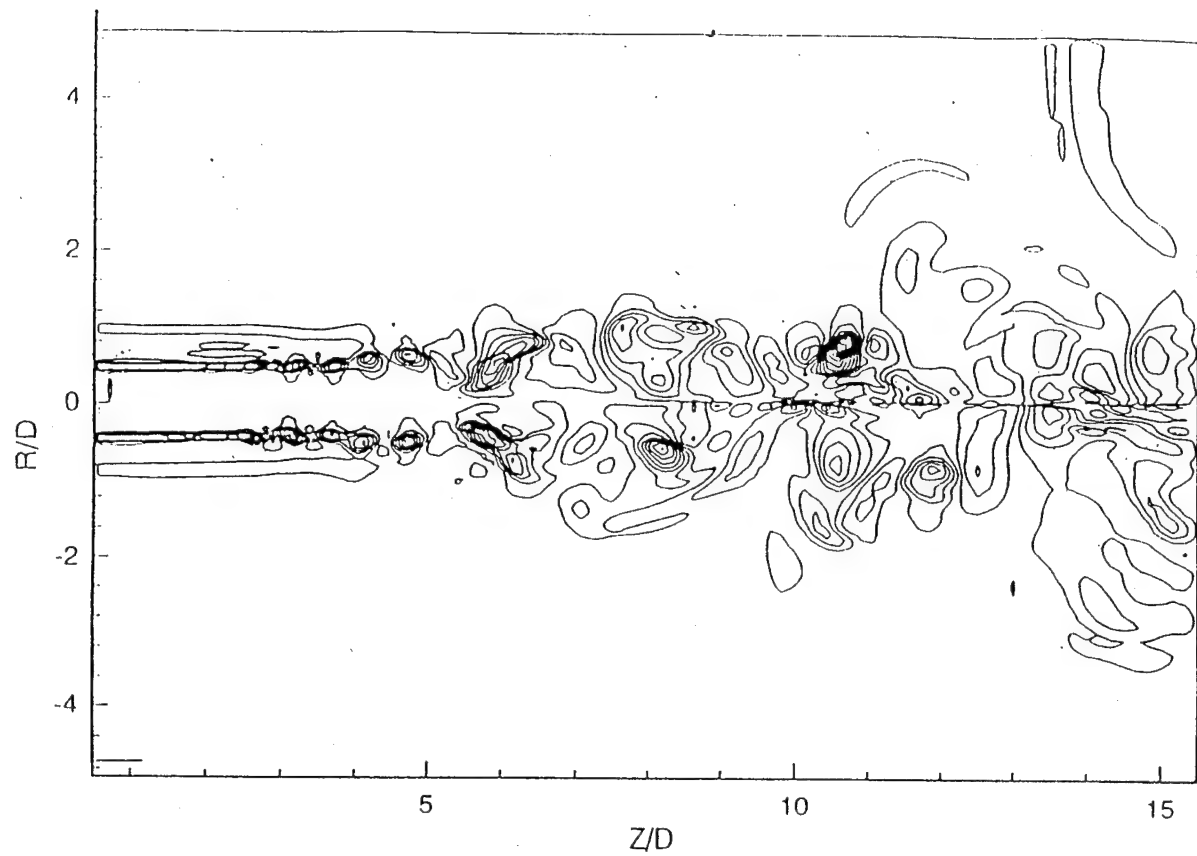


Figure 10: Same as figure 9 showing the full axial range.

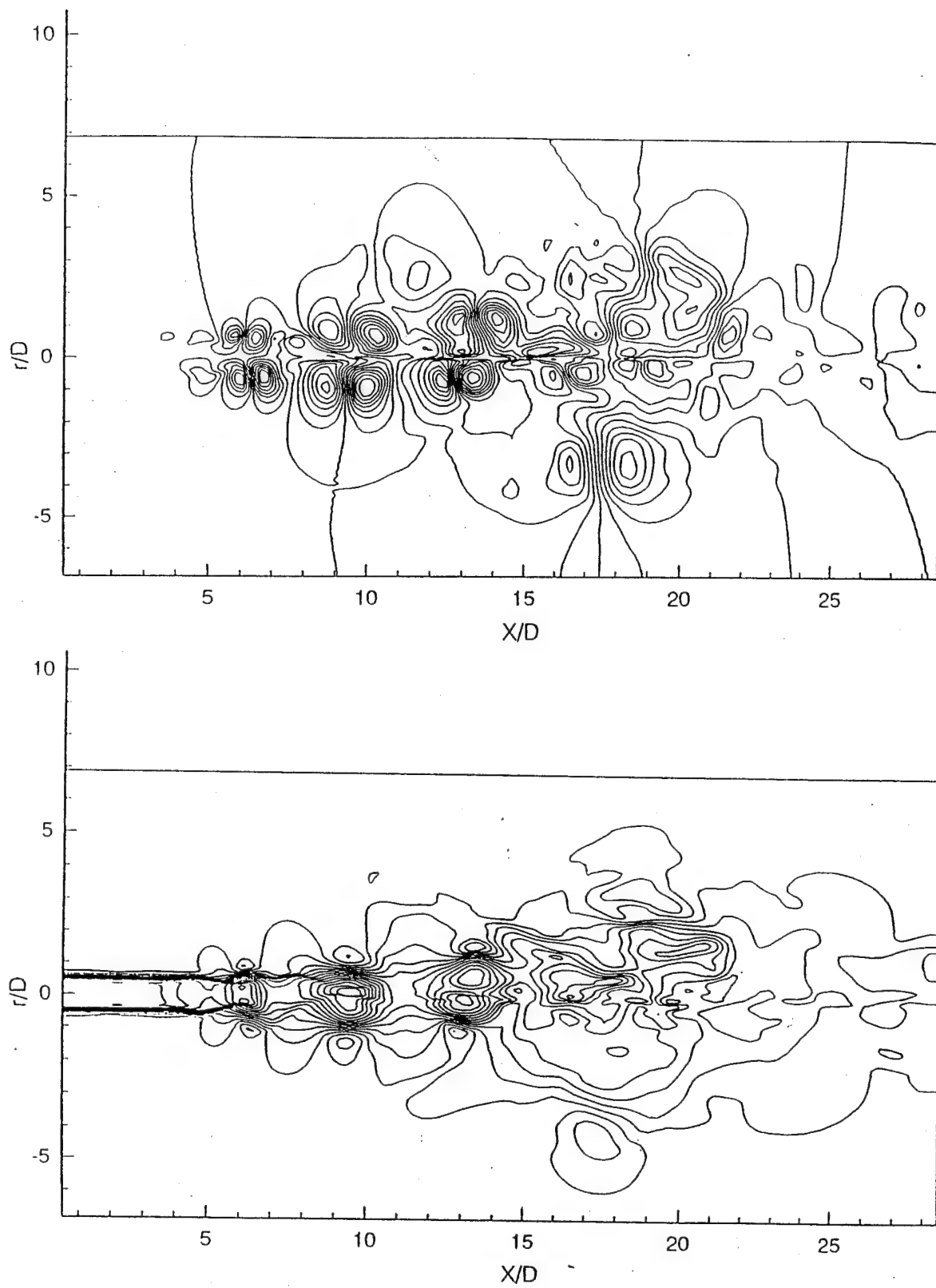


Figure 11: Longitudinal velocity component (lower graph) and radial velocity component (upper graph) iso-lines in the plane $\theta = 0/\pi$ for $Re = 13,000$ without the backscatter effect.

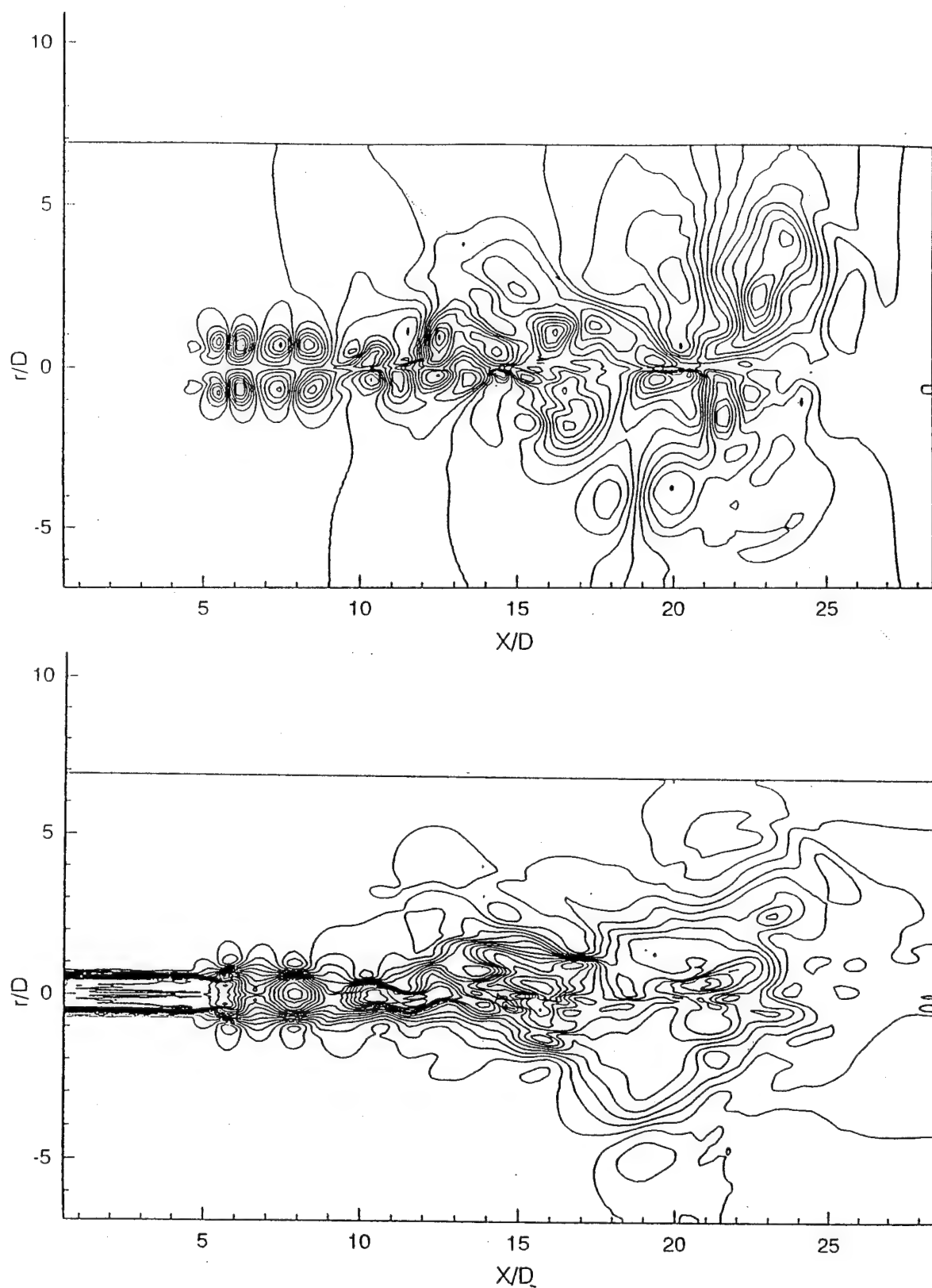


Figure 12: Same as figure 11 with backscatter effect.

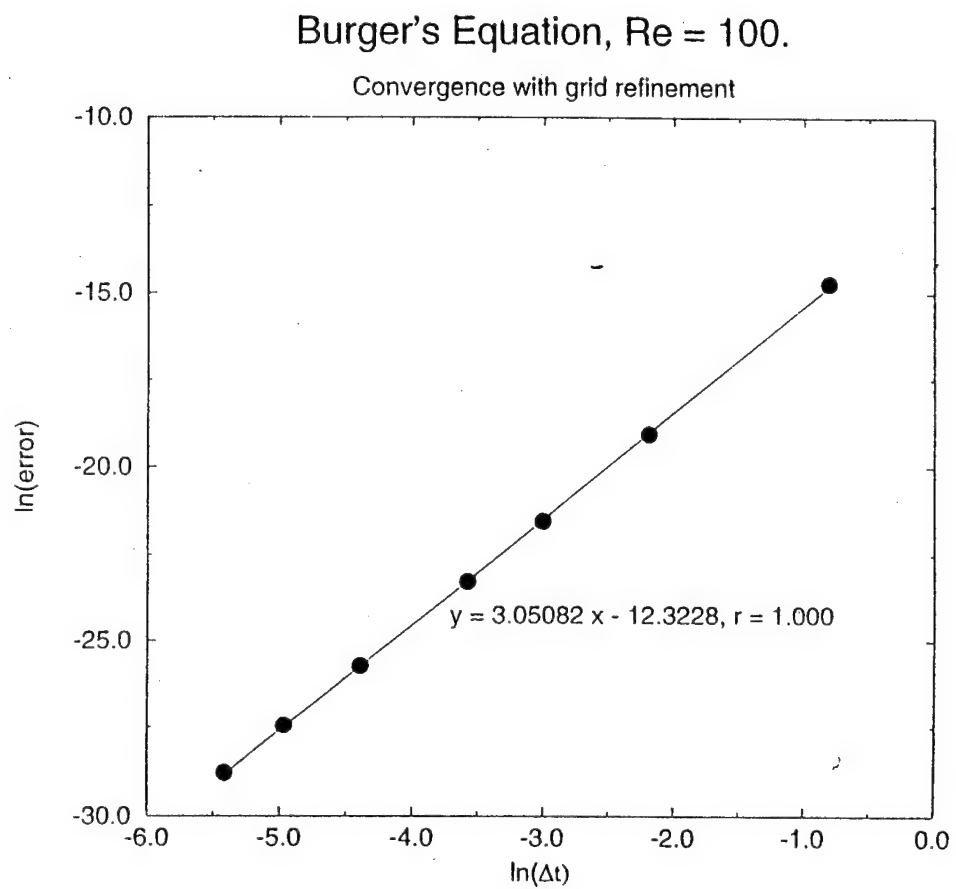


Figure 13: Time convergence of the third order Runge-Kutta time integration scheme and 6th order compact spatial discretization for the Burgers equation ($Re = 100$).

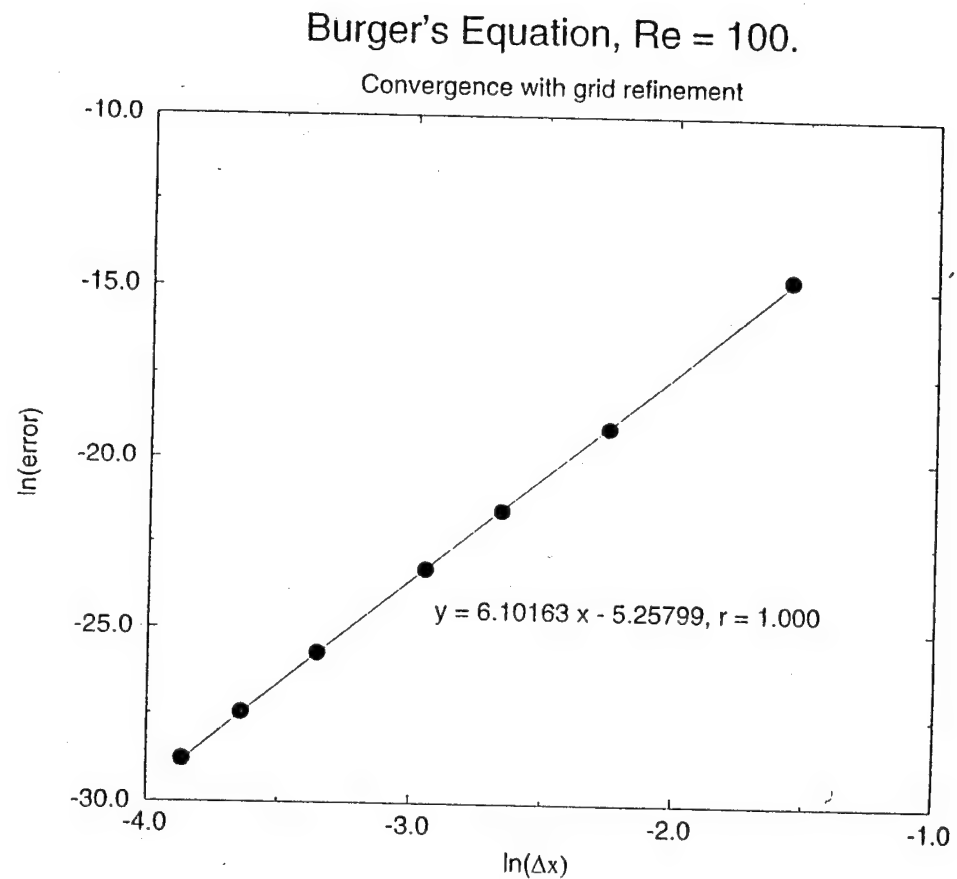


Figure 14: Spatial convergence of the third order Runge-Kutta time integration scheme and 6th order compact spatial discretization for the Burgers equation ($Re = 100$).

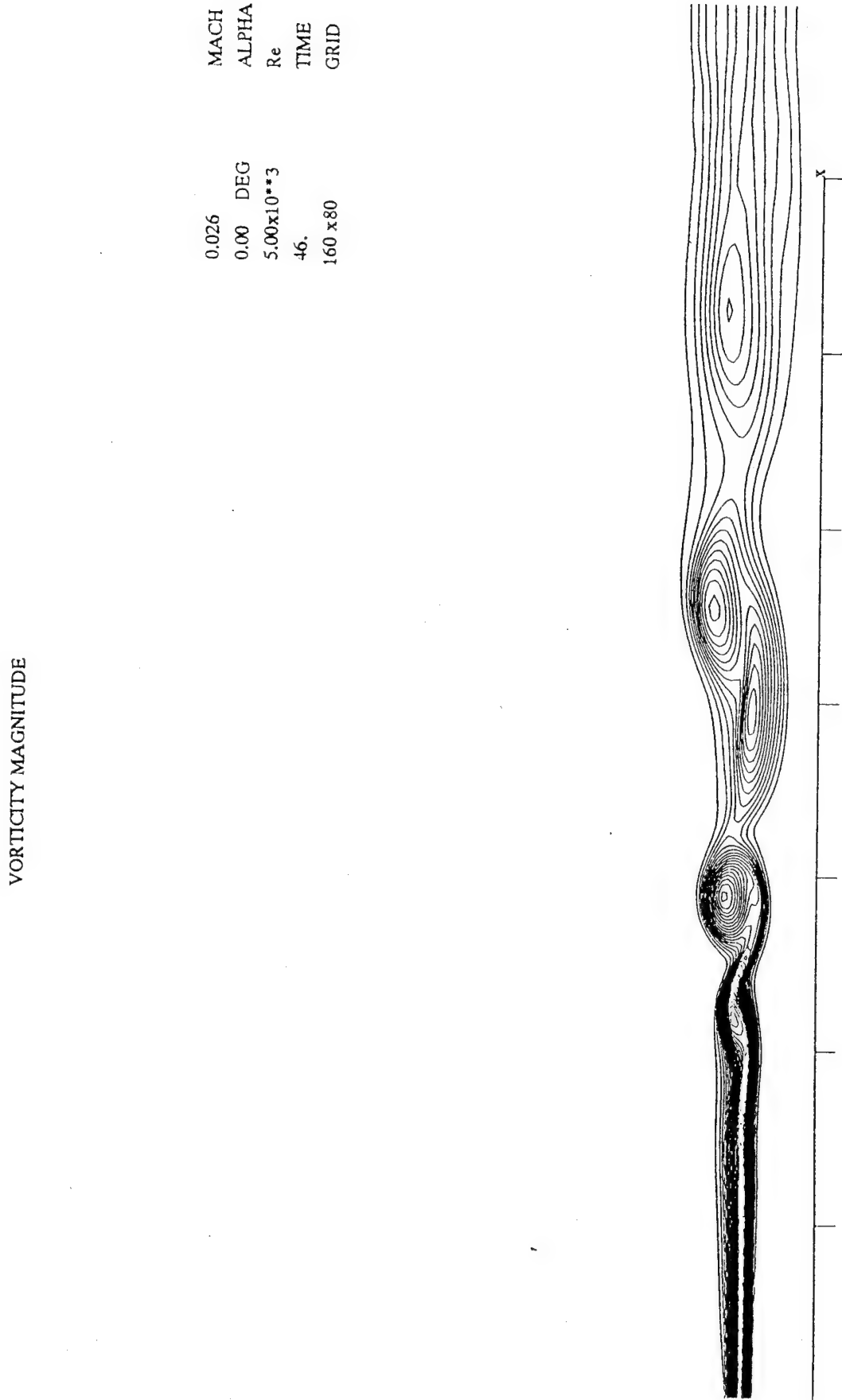


Figure 15: Vorticity magnitude for an axisymmetric round jet using the third order Runge-Kutta time integration scheme at $Re = 5000$ and $t = 46$.

Maximum Vorticity

3rd Order Runga-Kutta

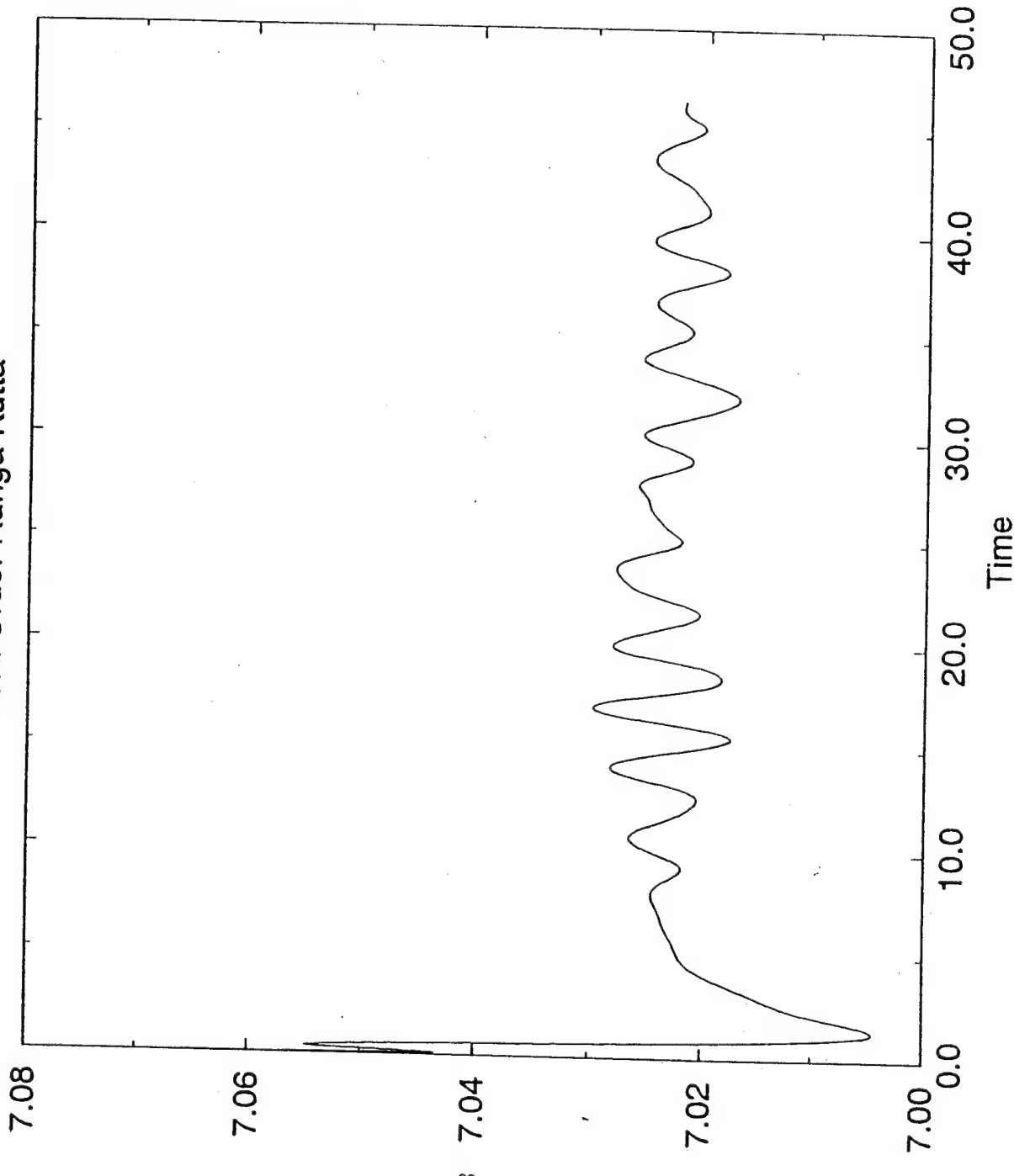


Figure 16: Time history for the maximum norm of vorticity for the flow in figure 15.

Divergence of Velocity

3rd Order Runge-Kutta

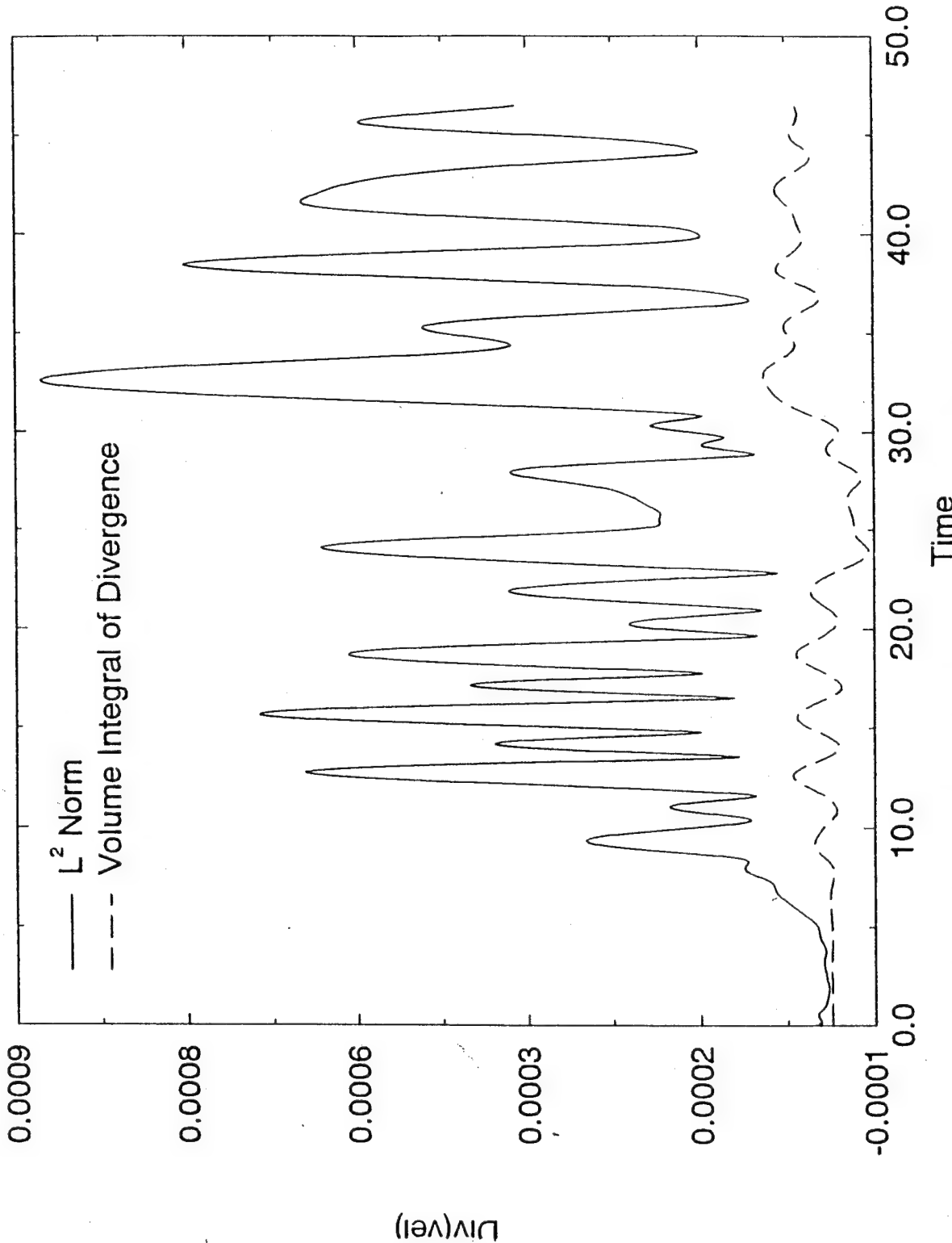


Figure 17: Time history of the L^2 -norm and the integral of the velocity divergence for the flow in figure 15.

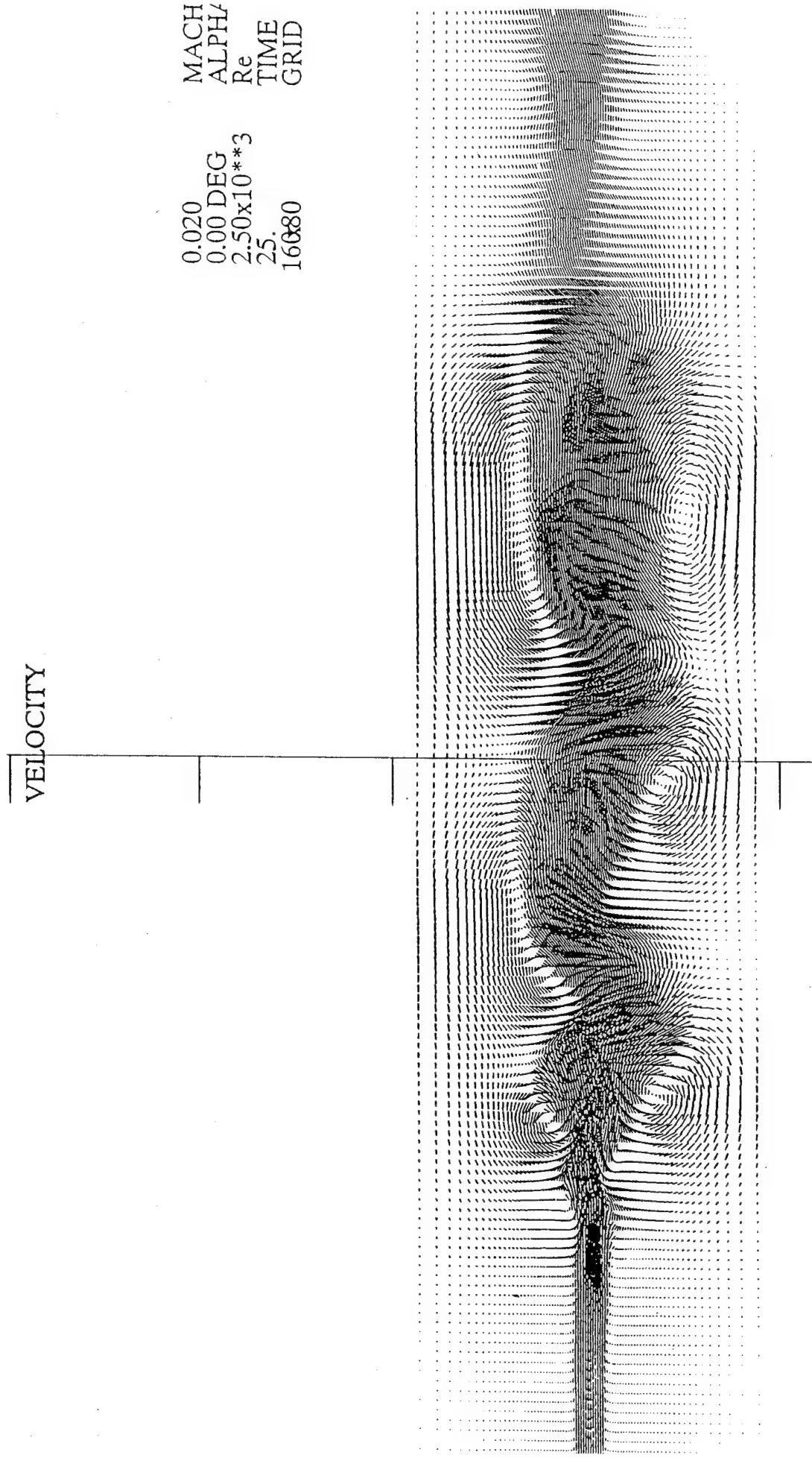


Figure 18: LES simulation of a plane jet using the fourth order Runge-Kutta time integration scheme and fourth order compact spatial discretization, velocity vectors for $Re = 2500$ at $t = 25$.

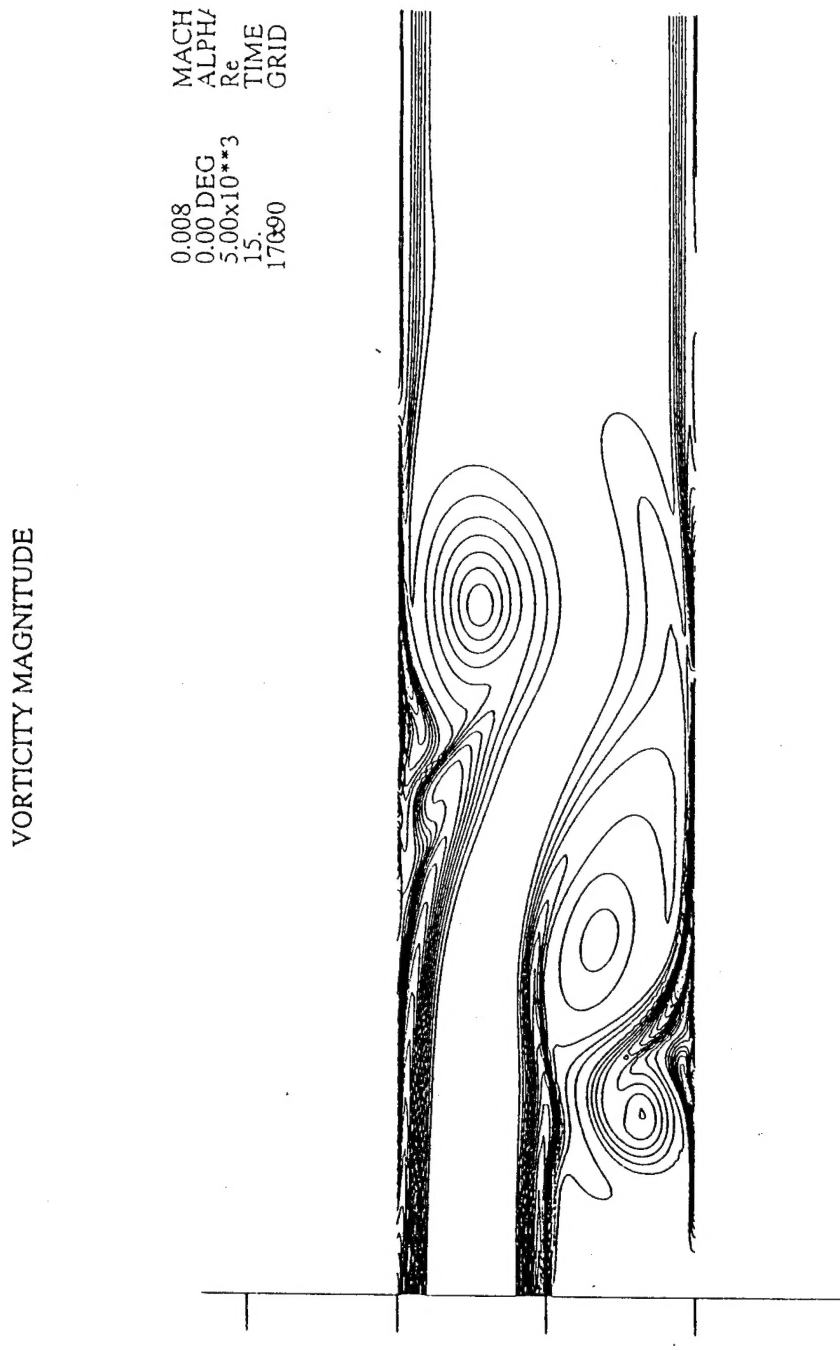


Figure 19: LES simulation of the backward-facing step flow using the fourth order Runge-Kutta time integration scheme, iso-lines of vorticity magnitude at $t = 15$ and $Re = 5000$ (based on step height).

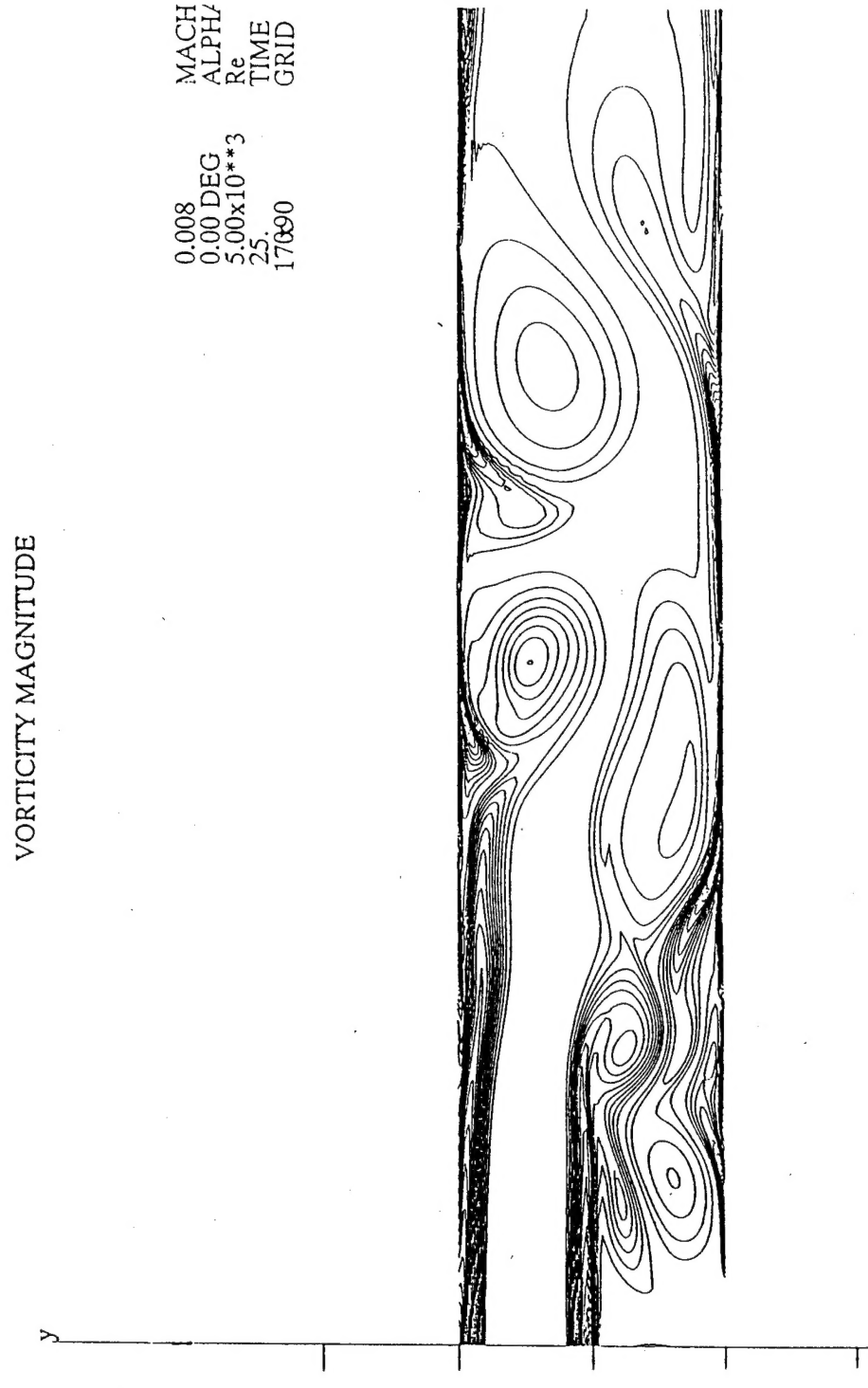


Figure 20: Same as figure 19 at $t = 25$.

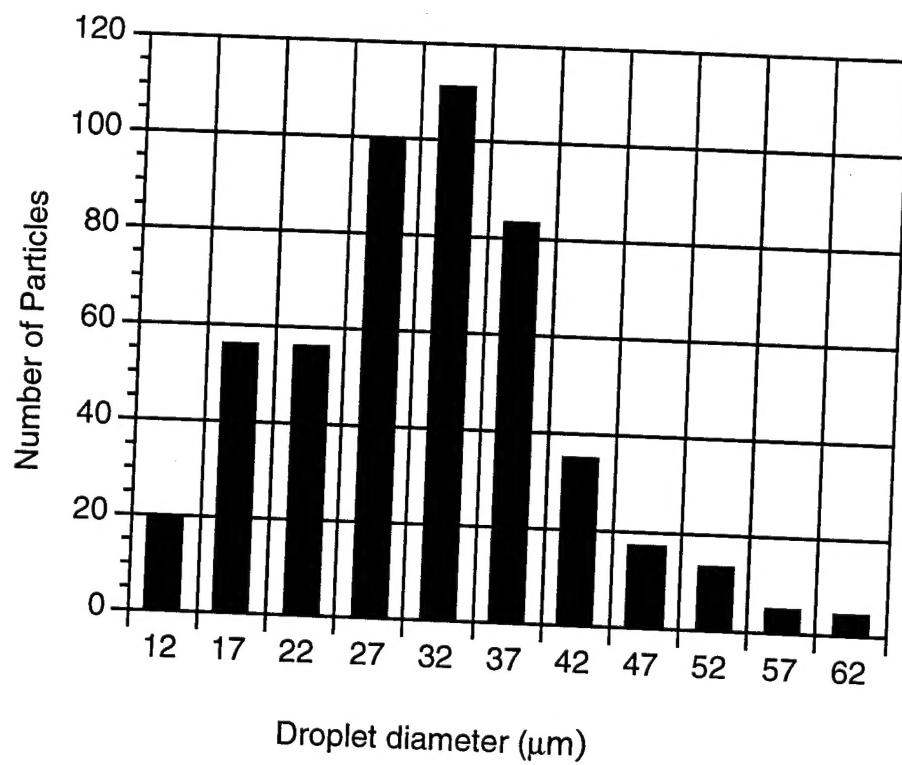


Figure 21: Spray size distribution.

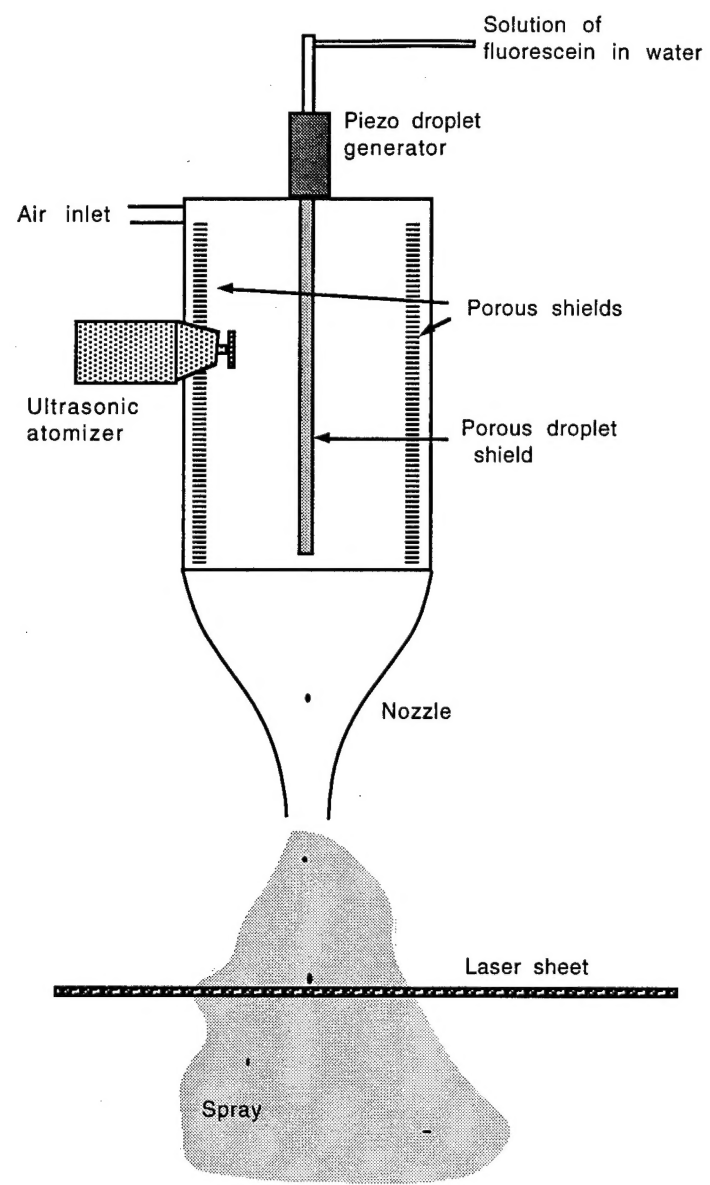


Figure 22: Apparatus for tracking fluorescent particles in a turbulent spray.